iScience

CellPress
OPEN ACCESS

Article

Small Groups, Big Impact: Eliminating Li^+ Traps in Single-Ion Conducting Polymer Electrolytes

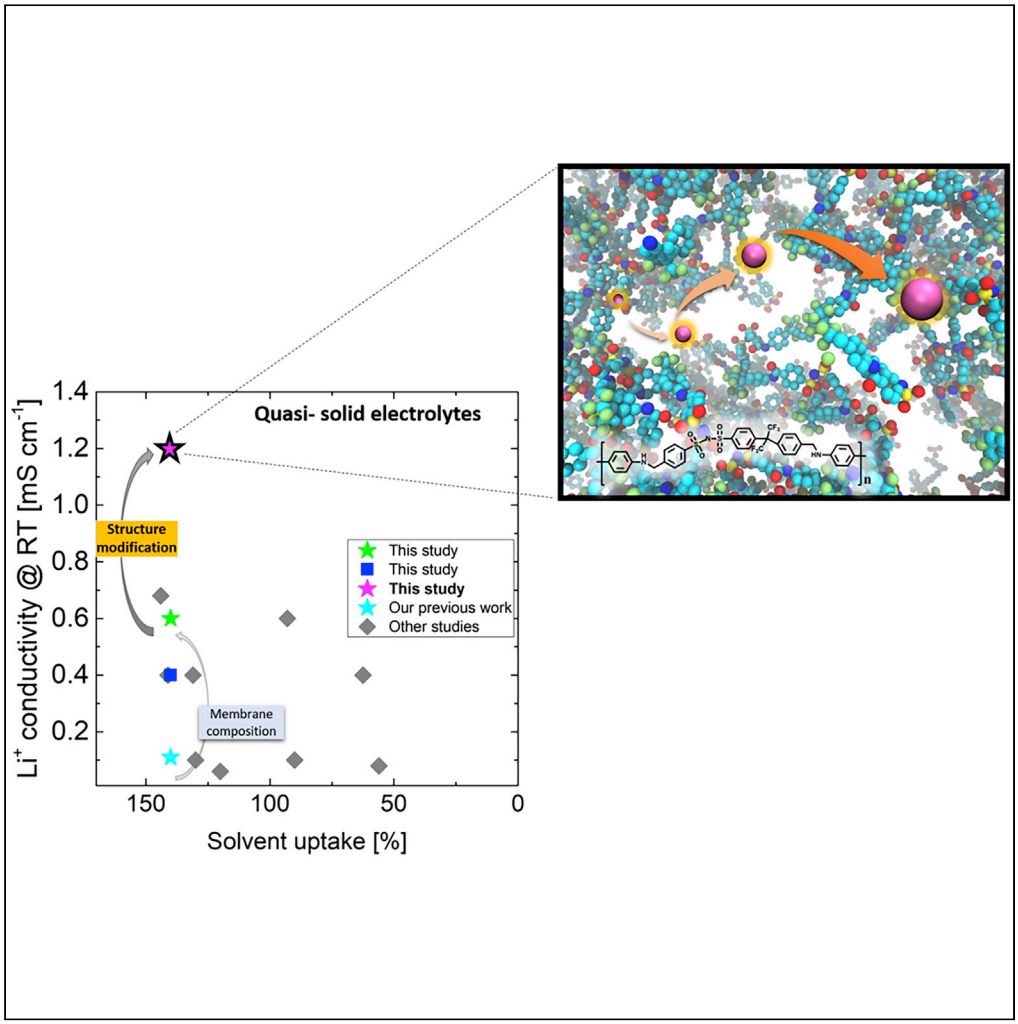

Kristina Borzutzki, Dengpan Dong, Christian Wölke, ..., Martin Winter, Dmitry Bedrov, Gunther Brunklaus

d.bedrov@utah.edu (D.B.)
g.brunklaus@fz-juelich.de (G.B.)

HIGHLIGHTS

Relations between polymer structure and charge transport properties are revealed

Identification of Li^+ "*traps*" in the polymer by combined MD simulations and experiments

Duplication of ionic conductivity by reduction of the polymer backbone

Change in membrane morphology by variation of a chemical group in the polymer backbone

Borzutzki et al., iScience *23*, 101417
August 21, 2020
https://doi.org/10.1016/j.isci.2020.101417

iScience

CellPress
OPEN ACCESS

Article

Small Groups, Big Impact: Eliminating Li^+ Traps in Single-Ion Conducting Polymer Electrolytes

Kristina Borzutzki,[1,5] Dengpan Dong,[2] Christian Wölke,[1] Margarita Kruteva,[3] Annika Stellhorn,[3] Martin Winter,[1,4] Dmitry Bedrov,[2,*] and Gunther Brunklaus[1,5,*]

SUMMARY

Single-ion conducting polymer electrolytes exhibit great potential for next-generation high-energy-density Li metal batteries, although the lack of sufficient molecular-scale insights into lithium transport mechanisms and reliable understanding of key correlations often limit the scope of modification and design of new materials. Moreover, the sensitivity to small variations of polymer chemical structures (e.g., selection of specific linkages or chemical groups) is often overlooked as potential design parameter. In this study, combined molecular dynamics simulations and experimental investigations reveal molecular-scale correlations among variations in polymer structures and Li^+ transport capabilities. Based on polyamide-based single-ion conducting quasi-solid polymer electrolytes, it is demonstrated that small modifications of the polymer backbone significantly enhance the Li^+ transport while governing the resulting membrane morphology. Based on the obtained insights, tailored materials with significantly improved ionic conductivity and excellent electrochemical performance are achieved and their applicability in LFP||Li and NMC||Li cells is successfully demonstrated.

INTRODUCTION

The abundant presence of portable electronics and upcoming transportation based on electric vehicles currently stimulates extensive research efforts to provide battery technologies with substantially increased electrochemical properties, environmentally less impacting chemistries, as well as enhanced cycle and calendar lifetime at affordable costs (Placke et al., 2017). Owing to the clearly conflicting demands, the corresponding materials design strategies are not straightforward, and despite the impressive progress achieved in the field of lithium ion batteries, an advancement to next-generation lithium-metal and so-called anode-free batteries requires a conceptual shift away from current liquid electrolytes, e.g., toward inorganic, polymer, or hybrid electrolytes (Janek and Zeier, 2016; Schmuch et al., 2018). Notably, practical application of polymer electrolytes with lithium metal electrodes was convincingly demonstrated by Blue Solutions, including Bluecar and Bluebus, although the achievable energy density of the lithium metal polymer (LMP) battery is strongly limited and considerably lower than that of state-of-the-art lithium ion batteries (LIBs), attributed to the low ionic conductivity and limited anodic stability of polyether-type polymer electrolytes and corresponding cathode material selection (Wu et al., 2019; Zhang et al., 2020). Such examples demonstrate that further efforts and substantial progress are required to improve currently available polymer electrolytes, making them suitable for lithium metal-based battery (LMB) systems that are attractive and competitive to conventional LIB technologies. Among the various strategies for the design of alternative polymer electrolytes that promote the achievable ionic conductivity, fabrication of single-ion conducting polymer electrolytes (SIPEs) is currently considered as particularly interesting to afford materials relevant for lithium metal-based batteries (LMBs) (Long et al., 2016; Zhang et al., 2017a, 2017b). SIPEs could enable enhanced cell longevity since build-up of undesired cell polarization, a major reason for a growth of inhomogeneous Li deposits and eventually short circuits of the cell, could be prevented (Chazalviel, 1990). SIPEs have been prepared via synthesis of block copolymers (where the ionic transport properties and membrane morphology are adjusted via different block sizes and constituents) or polymers with alternating anionic and non-ionic monomers, even including direct copolymerization of lithium salt monomers (Zhang et al., 2017a, 2017b; Deng et al., 2020). The resulting polymer electrolytes may be fabricated as solid electrolytes (often utilizing polyethylene oxide [PEO] as blend partner) (Meziane et al., 2011; Ma et al.,

[1]Helmholtz-Institute Münster, IEK-12, Forschungszentrum Jülich, Corrensstr. 46, 48149 Münster, Germany

[2]Department of Materials Science and Engineering, University of Utah, 122 S. Central Campus Dr., Rm. 304, Salt Lake City, UT 84112, USA

[3]Jülich Centre for Neutron Science (JCNS-1) and Institute for Complex Systems (ICS-1), Forschungszentrum Jülich GmbH, 52425 Jülich, Germany

[4]University of Münster, MEET Battery Research Center, Institute of Physical Chemistry, Corrensstr. 46, 48149 Münster, Germany

[5]Lead Contact

*Correspondence: d.bedrov@utah.edu (D.B.), g.brunklaus@fz-juelich.de (G.B.)

https://doi.org/10.1016/j.isci.2020.101417

2016) or "quasi-solid" electrolytes, in which substantially enhanced ionic conductivities are achieved upon addition of limited amounts (below 150 wt %) of salt-free, low-molecular-weight plasticizer(s) (Van Schalkwijk and Scrosati, 2002; Rohan et al., 2015; Long et al., 2016; Cheng et al., 2018; Jia et al., 2018a; Jia et al., 2018b). This is in contrast to gel-type polymer electrolytes that might incorporate up to 2,200 wt % of plasticizer(s) (Zhang et al., 2018; Zhong et al., 2019; Zhou et al., 2019). To date, merely a few quasi-solid SIPEs with a room temperature (RT) ionic conductivity of 1 mS cm^{-1} or higher are reported (Deng et al., 2017; Oh et al., 2016; Rohan et al., 2014), whereas other plasticized SIPE material classes including block copolymers(Nguyen et al., 2018) or blend-type compounds(Zhang et al., 2014a; Sun et al., 2014; Zhang et al., 2014b; Qin et al., 2015; Rohan et al., 2015; Liu et al., 2016; Pan et al., 2016; Zhang et al., 2017a, 2017b; Dong et al., 2018; Li et al., 2018; Chen et al., 2018; Li et al., 2019) do not accomplish ionic conductivities of more than 1 mS cm^{-1}. However, in case of poly(vinylidene difluoride-*co*-hexafluoropropylene) (PVdF-HFP) blended SIPE membranes (the materials class investigated in this work), several promising single ion conducting polymer structures were explored, considering variations of the anionic species attached to polymer backbone or side chains, the ratio of the blend constituents, the nature of plasticizer molecules, as well as concepts for membrane fabrication and solvent uptake (Table S1) (Sun et al., 2014; Zhang et al., 2014a, 2014b; Pan et al., 2015, 2016; Liu et al., 2016; Zhang et al., 2017a, 2017b, 2018; Dong et al., 2018; Li et al., 2019). Nevertheless, although different morphological features (e.g., represented by porous or rather dense membrane structures) were observed even for similar constituents and preparation procedures, the comparable transport properties (10^{-4} mS cm^{-1}@ RT) in case of all the membranes clearly indicate that rational design of polymer electrolytes with substantial improvement of charge transport properties remains challenging. Employing solely experimental attempts for materials development, the exploration space is often limited to selected choices of chemical motifs comprising variations of monomer combinations, that the importance of eventually non-considered moieties on the actually achievable materials performance may be missed, or even hampers straightforward and systematic comparison of the invoked structural variants, hence rendering the potential of these materials classes partially unexploited.

Since atomistic molecular dynamics (MD) simulations based on parameterized force fields (that are derived from quantum chemistry and/or experimental data) are often sufficiently accurate at affordable computational costs, they constitute a valuable tool to provide insights into details of the charge carrier transport mechanisms, considering, e.g., ion speciation, diffusion coefficients, and localized ion distributions, in addition to structural arrangements of the constituent atoms reflecting molecular phase separation or to some extent occurring morphologies of polymer electrolytes (Borodin and Smith, 2006a; Steinmüller et al., 2012; Ganesan and Jayaraman, 2014; Mogurampelly et al., 2016; Franco et al., 2019). So far, however, available computational studies of the charge carrier transport within polymer electrolytes focused primarily on polyether-type systems, neglecting other available polymer classes (Zheng et al., 2018; Franco et al., 2019; Gartner and Jayaraman, 2019; Ketkar et al., 2019). Critical parameters to evaluate the capability of Li^+ transport (as reflected by the bulk ionic conductivity) within a considered electrolyte comprise the transference number (which should be close to unity), the availability and valence of anionic moieties, the content of plasticizer(s), if any, as well as the chemical constitution, the underlying polymer structures (e.g., aromatic/linear backbone and, if present, side chain design, presence of chemical groups that interact with Li^+, the overall Li^+ concentration and degree of ion dissociation), and overall polymer morphology, including interconnectivity and percolation of charge transport channels. However, the interdependency of these parameters and, consequently, the complexity of ionic transport in combination with the overwhelming variety of different compounds and material classes investigated renders rational comparison and straightforward development even for compounds within the same material class highly challenging. Therefore, in this work, quasi-solid single-ion conducting polymer electrolytes suitable for application in LMBs are considered, clearly demonstrating the explicit roles of individual chemical entities governing the achievable bulk materials properties, including the macroscopic morphology (porosity) as well as ion transport properties. In particular, MD simulations complemented by experimental small angle X-ray scattering (SAXS) and Li^+ species transport data enabled accurate sampling of local charge carrier environments and dynamical correlations thereof, hence revealing underlying transport mechanisms while unambiguously highlighting that apparently negligible backbone modifications significantly affect the achievable ion transport properties.

RESULTS AND DISCUSSIONS

In most single-ion conducting polymer electrolytes, anions are either covalently anchored to the backbone or immobilized by neutral molecules ("anion acceptors") through classic Lewis acid-base theory (Zhang et al., 2017a, 2017b), so that the cationic species as major charge carriers are rather mobile despite their potentially strong electrostatic interactions with the anions. In the absence of plasticizers, ion motion

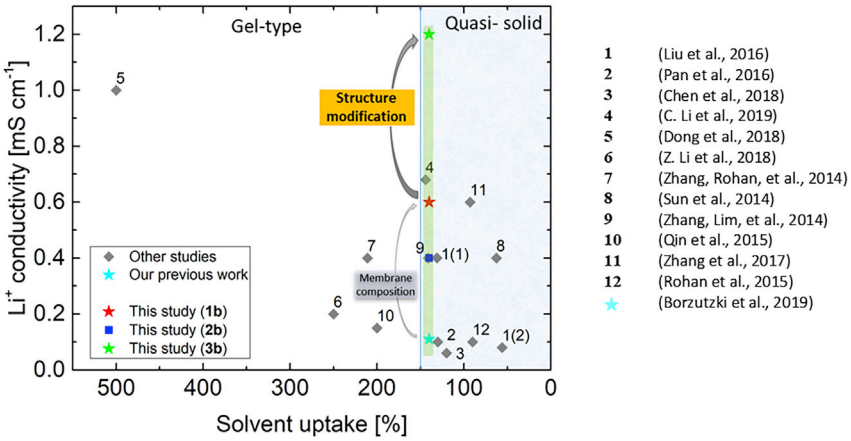

Figure 1. Ionic Conductivities of PVdF-HFP Blended SIPE Membranes as Function of Plasticizer/Solvent Uptake at Room Temperature

Only reports that allowed for meaningful comparison of the degree of solvent uptake and resulting lithium ion conductivities were considered, thereby regarding polymer blend electrolytes with solvent uptakes of ≤150 wt % as "quasi-solid." Particularly highlighted are the polymer electrolytes (**1b**), (**2b**), and (**3b**) introduced based on the proposed approach in this work.

mainly occurs via "hopping" processes, whereas for quasi-solid electrolytes, net charge transport due to translational diffusion of solvated Li^+ species likely (also) contributes to the achievable ionic conductivity of the SIPE, irrespective of the present polymer morphology. In cases where the mechanical stability of the respective polymer electrolytes is insufficient to allow for preparation of self-standing membranes, polymer blending may conveniently enhance the mechanical properties. Several different blend partners were suggested (Meziane et al., 2011; Ngai et al., 2016; Zhang et al., 2014a; Zhong et al., 2019), whereof PVdF-HFP is particularly known to impose excellent mechanical properties, as well as good thermal, chemical, and electrochemical stabilities, rendering it a highly favored blend partner for SIPEs (Zhang et al., 2014a, 2014b; Liu et al., 2016; Li et al., 2019). Notably, Figure 1 illustrates the actually achieved ionic conductivities at room temperature of previously reported SIPEs comparable with the quasi-solid blend membranes (**1b**), (**2b**), and (**3b**) of this work as a function of plasticizer/solvent uptake. All considered PVdF-HFP blended SIPE membranes exhibit different polymer architectures, solvent solutions, and membrane compositions (other major characteristics of the polymer blends are collected in Table S1, see Supplemental Information) (Zhang et al., 2014a; Sun et al., 2014; Zhang et al., 2014b; Qin et al., 2015; Rohan et al., 2015; Liu et al., 2016; Pan et al., 2016; Zhang et al., 2017a, 2017b; Dong et al., 2018; Li et al., 2018; Chen et al., 2018; Li et al., 2019). The obtained morphologies of polymer electrolyte membranes similarly prepared from solution casting varied from highly porous (micrometer-sized pores) (Sun et al., 2014; Zhang et al., 2014a, 2014b; Pan et al., 2015, 2016; Rohan et al., 2015; Zhang et al., 2017a, 2017b, 2018; Dong et al., 2018; Chen et al., 2018; Li et al., 2019) to rather dense structures (nanometer-sized pores), (Zhang et al., 2014a, 2014b; Qin et al., 2015; Liu et al., 2016; Pan et al., 2016; Li et al., 2018; Borzutzki et al., 2019), with no clear trend for different SIPE structures. Note, though, that a homogeneous membrane morphology is considered beneficial to prevent the formation of inhomogeneous high-surface-area ("needle-like" or "dendritic") lithium (HSAL [Winter et al., 2018]) deposits that otherwise could grow throughout the pore structures, eventually yielding short circuits within the cells (Zhang, 2018; Lagadec et al., 2019).

Owing to variation of multiple parameters, a straightforward correlation of observable transport phenomena and electrochemical properties of the materials were not attempted so far, although in our previous work, substantial improvement of the ionic conductivity was achieved in case of optimized blend membrane compositions, while increasing the exploited charge carrier density by 40% (Borzutzki et al., 2019) (turquoise and red stars in Figure 1, both reflecting materials with rather dense polymer morphologies). Clearly, an impressive improvement of ion transport properties could be achieved based on the proposed approach in this work (red and green stars in Figure 1), maintaining the beneficial dense membrane morphology, unambiguously highlighting that better understanding of charge carrier transport phenomena and intermolecular interactions within the considered polymer electrolytes indeed constitute powerful means for tailored design of functional materials.

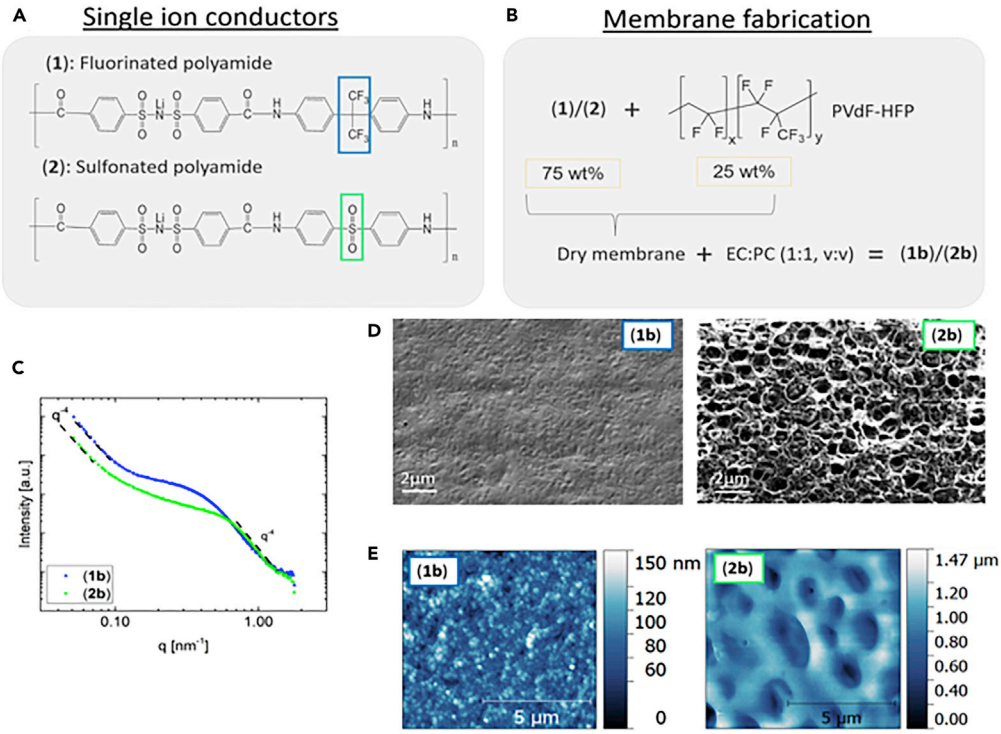

Figure 2. Structural Comparison of System (1) and (2)

(A) Chemical skeleton structures of the investigated single-ion conducting polymers, (B) schematic of the membrane composition, (C) SAXS data, (D) SEM images, and (E) AFM images of (**1b**) as well as (**2b**) at 298 (K).

Impact of Functional Groups on Membrane Morphology and Transport Properties

Physically blending two polymers offers convenient opportunities to modify materials. Blends typically acquire small-scale spatial arrangements (referred to as "microstructure") that critically affect the resulting ion transport or electrochemical properties (Shin et al., 2017). The impact of membrane morphology on ion transport properties was particularly studied in case of protonated polymer electrolyte membranes suitable for fuel cell application, where phase separation is utilized to induce formation of phase-separated nano-channels that improve ionic transport as well as mechanical properties, irrespective of the actual nature of the solvated charge carrier species. In contrast to solid polymer electrolytes, in which a lithium salt solvating polymer or a polymer block in combination with a second mechanically stiff compound enables the formation of continuous pathways for ion transport while ensuring mechanical stability (Sadoway et al., 2001; Trapa et al., 2002; Bouchet et al., 2013), multi-component polymer blends facilitate charge carrier transport networks via preferential incorporation of plasticizers/solvents into one (preferred) phase (either hydrophilic or hydrophobic) (Song et al., 1999; Shin et al., 2017; Nguyen et al., 2018). Hence, nano-phase separation in polymer electrolytes is rather beneficial for effective ionic transport compared with systems in which two block segments are intermixed (Sadoway et al., 2001; Trapa et al., 2002; Bouchet et al., 2013).

Herein, the single ion conducting compounds (**1**) or (**2**) (Figure 2A), which purposely differ solely in a single functional group, where (**1**) includes $C(CF_3)_2$ moieties (Borzutzki et al., 2019), whereas (**2**) has SO_2 units within the polymer backbone (Zhang et al., 2018; Li et al., 2019), and PVdF-HFP were consulted for preparation of the blend membranes. As depicted in Figure 2B, the dry membranes produced by solution casting were plasticized in EC:PC (1:1, v:v), yielding (**1b**) and (**2b**). Thereby, based on our previous study in which optimization of the membrane composition with respect to their final morphology and ion transport properties was investigated (Borzutzki et al., 2019) the corresponding blend membranes were prepared with a polymer ((**1**) or (**2**)) to PVdF-HFP ratio of 3:1 and subjected to comparable plasticizer/solvent uptake of 140 wt %, (**1b**), and 150 wt %, (**2b**), respectively. The stated solvent amounts reflect the natural solvent uptake determined by the membrane weight after saturation is reached upon swelling. Note that natural solvent uptake was also identified as optimal solvent content within the experimentally accessible uptake range (cf.

Supplemental Information). Less solvent uptake reduced the achievable ionic conductivity, whereas attempts to exceed the natural solvent uptake resulted in volume expansion and partial dissolution of the polymer membrane. In case of (**1b**), changes in ionic conductivity for either 142 or 148 wt % were negligible (Figure S1B), so that a comparison of (**1b**) and (**2b**) was feasible, including the charge transport properties of both quasi-solid polymer electrolytes.

Figures 2C–2E display the morphological features of the membranes on micrometer and nanometer scales based on small-angle X-ray scattering (SAXS), scanning electron microscopy (SEM), as well as atomic force microscopy (AFM). In particular, SAXS data (Figure 2C) reveal a broad peak for both membranes, indicating a (partially) phase-separated structure of the polymer blends (Oikonomou et al., 2015; Chen et al., 2017a, 2017b). Since a clear scattering peak is observed for pure PVdF-HFP films, whereas no scattering peak was found for pure (amorphous) membranes of (**1**) (Figure S2), all scattering features for the blend membranes reflect individual domains of crystalline PVdF-HFP, which are still present in the considered blend membrane, as also demonstrated by XRD data (Figure S3). In agreement with both, a shift of the glass transition temperature T_g determined for these materials (Zhang et al., 2018; Borzutzki et al., 2019) and previous data of PVdF-HFP-based polymer blends produced by solution casting, the SAXS data in Figure 2C clearly is consistent with phase separation of crystalline PVdF-HFP and intermixed amorphous phases composed of single-ion conducting polymer and amorphous fractions of PVdF-HFP (Oikonomou et al., 2015; Chen et al., 2017a, 2017b). Note that the presence of an intermixed phase is also supported by interactions between (**1**) and (**2**) with PVdF-HFP, as indicated by characteristic shifts in the Fourier transform infrared (FTIR) spectra corresponding to SO_2, C=O, CH, and NH (Supplemental Information, Figures S4 and S5). The observable phase separation is induced by the applied solution casting process, since a corresponding SAXS peak can already be observed in the spectrum of a dry membrane (Figure S1A). Upon swelling, the scattering peak shifts to lower q values owing to broadening of the solvent channels. The correlation distance is larger for (**1**), in particular 16.2 nm (0.38 nm^{-1}) compared with 10.64 nm (0.59 nm^{-1}) for (**2**). For both systems, in the high q region, the Porod exponent (q^{-d}) describing the interphase and fractal dimensions of the scattering objects (Hammouda, 2008) yields d = 4, reflecting sharp interphases between crystalline PVdF-HFP and intermixed blend domains (Cornet et al., 2000; Nguyen et al., 2018). In addition, for both systems, strongly increasing intensities (close to Porod's law) in the low q region are indicative of micron-sized grains or clustering (Nguyen et al., 2018; Hammouda, 2008) These results are similar to recent observations in case of quasi-solid single-ion conducting block copolymers, demonstrating that the morphologies of phase-separated systems composed of either block copolymers or physically mixed blends are rather comparable (Nguyen et al., 2018).

Although the phase segregation on a nanometer scale (SAXS) is comparable for the membranes (**1**) and (**2**), significant differences of the membrane morphology on the micrometer scale is evident from SEM data (Figure 2D), where (**1**) displays a mostly homogeneous morphology without distinct features, whereas micrometer-sized pores are readily visible in case of (**2**). AFM images in Figure 2E illustrate that even in (**1**) clusters of 200 nm (data analysis via *ImageJ*) are present, consistent with the trend of the SAXS curves in the lower q region. This indicates different extents or "tiers" of clustering (comprising macromolecular nodules at first, followed by formation of nodule aggregates and finally super-nodular aggregates [pores] provided that strong separation is induced) (Kesting, 1990), upon fabrication of polymer electrolytes with different chemical moieties, thereby strongly emphasizing the significance of these entities for the resulting membrane morphology. Based on careful consideration of porous membranes obtained by similar polymers (Sun et al., 2014; Zhang et al., 2014a, 2014b; Pan et al., 2015; Liu et al., 2016; Zhang et al., 2017a, 2017b, 2018; Dong et al., 2018), it was postulated that polymer blends composed of aromatic SIPEs and linear polymers generally should result in rather porous membranes, hence recommending utilization of linear monomer units in SIPEs for a successful fabrication of homogeneous membranes (Zhang et al., 2014a, Zhang et al., 2014b; Liu et al., 2016). Although the impact of polymer architecture on the actual membrane morphology is of significant technological interest in case of many blends and block copolymers (Onorato and Luscombe, 2019), the explicit impact of the variation of backbone moieties has not been discussed so far. Therefore, computational and experimental (FTIR spectroscopy) investigations (Figures S4 and S5) were performed to determine the degree of intermolecular bonding between the blend partners. CF-HN intermolecular bonding (Gao and Scheinbeim, 2000; Yoon and Kim, 2000) is present in both systems, also O=S=O- HN interactions between different polyamide chains in (**2b**), indicating that strong specific intermolecular interactions between the considered blend partners can be excluded as origin of macro-sized pores. Rather, the observable phase separation results from the polarity of present chemical

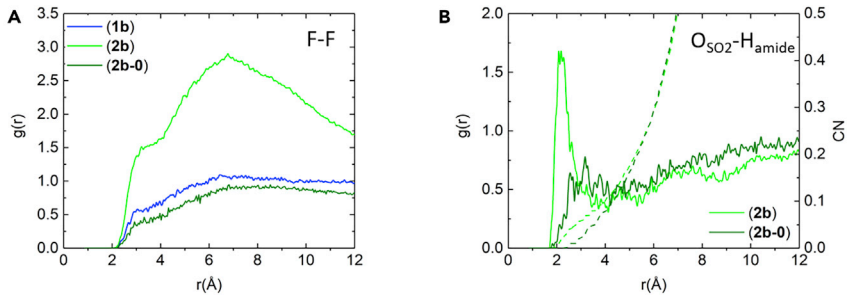

Figure 3. Structural Correlation in (1b) and (2b) with (2b-0) Being a Derivative System of (2b), in which the S-O Dipole Moment Is Scaled to Zero

Comparison of (A) F-F interactions of PVdF-HFP and (B) O_{SO2}-H_{amide}.

moieties (-SO_2 is highly polar, -CF_3 and PVdF-HFP are less polar) and is induced/enforced by solvent polarity gradients occurring upon solution casting. During membrane drying and evaporation of polar solvents, stronger phase separation of (**2**) and PVdF-HFP compared with (**1**) and PVdF-HFP occurs (Chen et al., 2017a, 2017b).

Although SEM and SAXS reveal meso- or micro-scaled structural features of polymer membranes, they are not sufficient for sampling of local/molecular-scale structures relevant to lithium ion coordination. In contrast, atomistic MD simulations with polarizable force fields quite accurately capture local structures and charge carrier dynamics in polymers (Bedrov et al., 2019) and hence were employed. Although MD simulations cannot access the micrometer scale to resolve the morphology of *entire* polymer membranes, nanometer-segregated structures inside SIPE-rich phase (with similar characteristics from SAXS for (**1b**) and (**2b**)) that primarily define Li transport can be readily accessed on time scales sufficient to reliably sample the lithium ion dynamics relevant for the bulk charge transport. The MD data reveal correlations consistent with the phase separation observed in experimental data, where the F-F radial distribution function (RDF) of (**1b**) (Figure 3) exhibits no observable structural correlation, i.e., no aggregation, whereas a wide RDF peak is observed in (**2b**), reflecting substantial aggregation of PVdF-HFP and phase separation from the anionic polymer (SIPE). Note that hydrogen bonds between O_{SO2} and H_{amide} provide additional attraction between anionic polymer segments, further enhancing phase segregation. Representative snapshots of the simulated systems (**1b**) and (**2b**) are shown in Figure 4, highlighting Li^+ that are "bound" (blue) and those considered as "free" (purple). Note that Li^+ ions with at least one anionic, amide, or sulfone oxygen atom in their first coordination shell are referred to as bound to the polymer at any given time, whereas those coordinated solely by oxygens from carbonate solvent molecules are termed free, since they represent the mobile charge carriers responsible for the observable ionic conductivity.

The snapshots clearly illustrate nanoscale segregation between plasticizer/solvent and the polymer phases, with the latter showing some regions of PVdF-HFP clustering as well as regions of intermixing of the two polymers, in good agreement with SAXS data. MD simulations show that Li^+ ions stay away from the regions occupied by PVdF-HFP chains and primarily coordinate diphenyl amide units or partition to the carbonate solvent-rich domains. The RDFs, *g(r)*, were calculated using MD trajectories to explore local structural correlations of Li^+ ions and their coordinating species. The correlations between Li^+ ions and oxygen atoms of anions (SO_2-N^--SO_2) $g_{Li^+-O_{anion}}(r)$, between Li^+ and double-bonded oxygen within amide groups of the polymer backbone (CO-NH) $g_{Li^+-O_{amide}}(r)$, between Li^+ and solvent double-bonded oxygen atoms $g_{Li^+-O_{solvent}}(r)$, as well as between Li^+ and the sulfone oxygen atoms (SO_2, only in (**2b**)) $g_{Li^+-O_{sulfone}}(r)$ obtained from simulations at 300 K are shown in Figure 5A. The *g(r)* for other temperatures are collected in the Supplemental Information (Figure S6), although the actual impact of temperature on *g(r)* is not significant. The first solvation shell of Li^+ ion by oxygen atoms can be defined as first minimum in the corresponding *g(r)* (at ~2.9 Å for all types of oxygen atoms); the corresponding number of oxygen atoms within the Li^+ first coordination shell for both compounds is shown in Figure 5B. Note that the total number of oxygen atoms within the first coordination shell of the Li^+ ion is ≈4, independent of solvent concentration or the nature of single-ion conducting polymer (Figure S6), similar to carbonate-based bulk solvent mixtures (Borodin and Smith, 2006b). In (**1b**), as anticipated, the higher solvent content results in an increased coordination of Li^+ by solvent molecules and reduction of coordination by oxygens of the anionic polymer (SIPE), hence affording enhanced ionic conductivities (Figure S1B), whereas in (**2b**), there is a slight increase

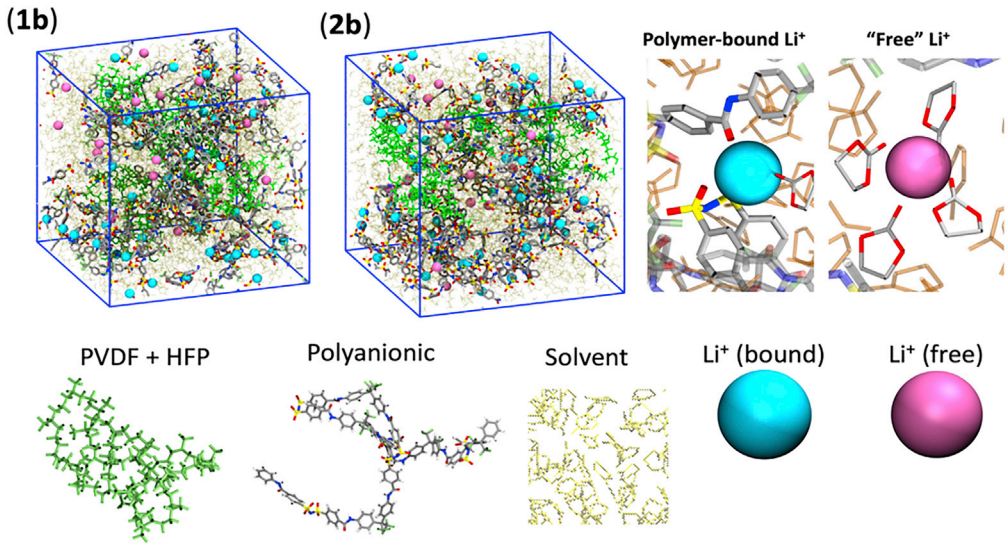

Figure 4. Snapshots of (1b) and (2b) Obtained from MD Simulations Illustrating Polymer-Bound and Free Li^+ Ions as well Illustrating the Heterogeneity of SIC Structure

in coordination of Li^+ with anionic oxygens as well as with solvent molecules and noticeably less binding with the amide oxygen in the backbone, while merely a small fraction of sulfone oxygen atoms coordinates to Li^+. Figure 5C illustrates the solvation structure of Li^+ with respect to the number of coordinating oxygen atoms corresponding to EC or PC molecules. The x and y axes show the number of oxygen atoms from PC and EC, respectively, whereas the color represents the probability of their occurrence N_o. The likeliest constellation is $Li^+EC_1PC_1Polymer_x$ (ca. 27%) with Li^+ being coordinated to *one* EC and *one* PC molecule while being additionally coordinated to the polymer. Coordination of Li^+ to *two* EC and *two* PC molecules represents the second most probable scenario (18%, most of them might be $Li^+EC_2PC_2$ reflecting completely solvated Li^+ ions). Solvation by more than *four* oxygen atoms is rare, and solvation by either only EC or only PC is not observed. Indeed, the solvation behavior with respect to EC and PC is almost identical (symmetric coloration regarding the "slope 1" line in Figure 5C), which implies that, for Li^+, oxygen atoms corresponding to EC are non-distinguishable from oxygen in PC. This observation is reasonable owing to the similarity in the chemical structure of both solvent molecules.

Notably, MD data predict a fraction of ≈32% of "free" Li^+ in (**1b**) membranes (in agreement to experimental data) (Borzutzki et al., 2019) and 26% of free ions in (**2b**) (at solvent uptakes of 140 and 150 wt %), respectively. The fraction of free Li^+ at different solvent contents can be found in Figure S7; this classification is based on structural correlations. As experimental counterpart to determine and quantify Li^+-anion and Li^+-solvent interactions, as well as for verification of simulated data, IR and Raman spectroscopy in principle constitute powerful tools, yet it was demonstrated even in case of plain Li-salt/EC and Li-salt/PC systems that quantitative evaluation of Li^+ speciation based on corresponding IR/Raman peak assignments remains ambiguous (Allen et al., 2014). Considering highly functionalized polymers with many different functional groups, explicit separation of individual contributions of present moieties is even more challenging, owing to commonly strong overlap of spectroscopic signals, so that both Li^+ speciation and intermolecular interactions cannot be reliably quantified by spectroscopic data. However, a clear trend of higher degrees of ion dissociation could be observed at higher plasticizer/solvent contents of the polymer electrolytes (Figures S8–S10). In addition to structural features, dynamical properties of (**1b**) and (**2b**) were examined, particularly in view of the significant fraction of Li^+ ions that interact with the anionic polymer (O_{anion}, O_{amide}, and O_{SO2}), thereby assessing how long each coordinating atoms/species stay within the Li^+ coordination shell(s). The corresponding kinetics can be analyzed via calculation of residence times (τ) of Li^+ close to oxygen atoms (within the first coordination shell), as shown in Figure 6A, although detailed descriptions of the calculation procedure and residence times in different solvent content are summarized in the Supplemental Information (Figure S11). $\tau_{Li-O_{anion}}$, $\tau_{Li-O_{sulfone}}$, and $\tau_{Li-O_{amide}}$ are on the order of several nanoseconds, which is significantly (from a factor of 6 to more than an order of magnitude) larger than $\tau_{Li-O_{solvent}}$. Although the strong binding of Li^+ to anionic units is expected, the comparably strong binding

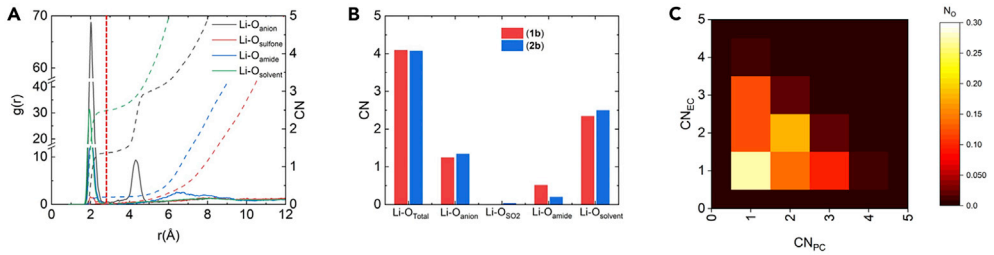

Figure 5. Analysis of Li^+ Coordination in System (1b) and (2b)

(A) Li^+-oxygen radial distribution function (solid lines) and coordination numbers (dashed lines).

(B) The average number of oxygen atoms within Li^+ first coordination shell.

(C) Probability (color scale) of different solvation structures (number of coordinating oxygen atoms from EC and PC molecules) of Li^+.

to amide linker oxygen atoms as well as to SO_2 groups in (**2b**) was not obvious *a priori*. Considering that less than 10% of the overall Li^+ ion transport occurs along the polymer backbone (Figure S12), higher fractions of bound Li^+ and long residence times within the first coordination shell of both types of oxygen atoms can critically limit the achievable lithium ion conductivity of the polymer blend electrolyte. Conductivity values calculated from MD simulations and experimentally obtained data presented in Figure 6B show an excellent agreement for both systems. (Note that simulations utilizing non-polarizable force fields are typically off from experimental results by almost an order of magnitude [Bedrov et al., 2018].) Moreover, the slopes of temperature-dependent ionic conductivities are consistent between MD simulations and experiments, thus further corroborating that the actual activation energy for Li^+ diffusion is accurately captured by MD data. As anticipated by the observations of Li^+ ion association, the degree of ion dissociation in (**2b**) is reduced, yielding a lower ionic conductivity σ_{Li^+} by 22% in simulations and by 28% in experiments compared with (**1b**).

Clearly, a reduction of bound Li^+ fractions and/or weakening of binding between Li^+ ions and polymer backbone moieties are highly adequate pathways to increase the achievable lithium ion conductivity of the considered class of quasi-solid polymer electrolytes. In view of long residence times of Li^+ ions near amide groups and no importance of this group to any other aspects of battery performance, an elimination of amide groups from the polymer backbone should enhance the Li^+ mobility without compromising the excellent cell performance of the SIPE membranes. This hypothesis was first explored in MD simulations, where modification of (**1b**) was mimicked by rescaling the dipole moment of the amide group of the initial system, thereby weakening interactions among amide units and Li^+ while keeping all other properties (polymer chain lengths and membrane composition) of the polymer blend system constant. The scaling of amide dipole groups to 25% of its original value effectively is equivalent to a replacement of the strongly polar C=O group with CH_2 achieved by chemical reduction of the protonated amide (**1-H**) using LiAlH4 thereby yielding (**3-H**) and subsequent lithiation to (**3**) as shown in Figure 7A. MD simulations demonstrated that, in the (**3b**) equivalent membrane, the polymer backbone has a very similar distribution of conformations and the resulting membrane morphology appears very similar as in case of (**1b**). All the changes in Li^+ coordination number within the first coordination shell are detailed in Figure 7B, reflecting that strong Li^+ binding/coordination to amide groups present in polymer (**1b**) is fully absent in (**3b**) (see, e.g., Li-C_{linker} coordination), while Li^+ coordination with anion and solvents is promoted. The distribution of different solvation structures (EC versus PC molecules) of Li^+ remains similar to (**1b**) and is displayed in Figure S6H. The head-to-head comparison of Li^+ residence times near the anions, solvents, and linker groups in (**1b**) and (**3b**) is presented in Figure 7C; residence times of Li^+ within the first Li^+-O_{anion} and Li^+-O_{sol} coordination are comparable, whereas the difference in residence near the C_{linker} drops by two orders of magnitude.

As a result, the MD simulations of (**3b**) equivalent membrane indicated enhancement of the free Li^+ fraction by 40%, accompanied by a higher self-diffusion coefficient of $D_{Li+} = 12.2*10^{-11}$ m^2s^{-1} in (**3b**) compared with $D_{Li+} = 8.6*10^{-11}$ m^2s^{-1} in (**1b**), reflecting an increase by 41.8%. The anticipated ionic conductivity σ_{Li^+} is significantly increased (by 47%) when the dipole moment of amide groups in (**1b**) is scaled down to merely 25% of the "original" value, in this way approximating the blend polymer electrolyte (**3b**). These data clearly highlight that C=O moieties within the polymer backbone act as Li^+ "traps" and should be preferentially

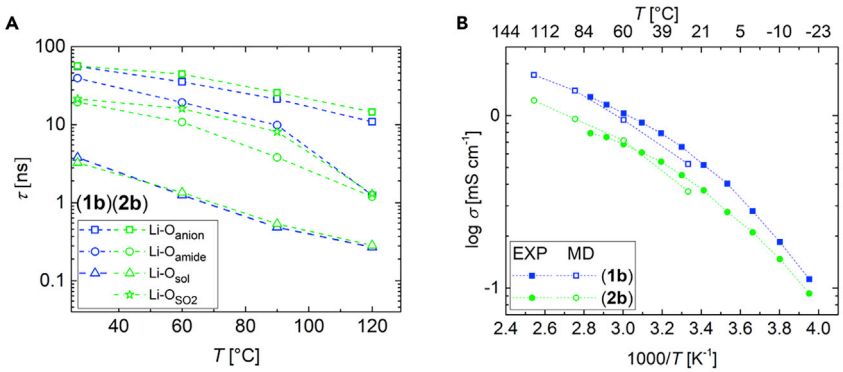

Figure 6. Li^+ Ion Transport-Related Properties in (1b) and (2b)

Temperature dependence of (A) Li^+ coordination residence times and (B) Ionic conductivity of polymer membranes. Closed symbols: experimental data (EXP), open symbols: simulated values (MD).

avoided to release bound Li^+ ions, in this way boosting the fraction of free Li^+ (merely solvated by carbonates) that mainly contributes to the charge transport within the respective polymer electrolytes. Experimentally, different options are available to reduce or avoid the presence of C=O functional group within the polysulfonamide backbone. In particular, other monomers containing, e.g., -OH and -F or -OH and -Cl end groups, yielding polyaryleneethers (McGrath et al., 2002; Chen et al., 2017a, 2017b) could be considered, although a more straightforward approach comprises modification of the polymer. As presented in Figure 7A, a single Li ion conducting polysulfonamine (**3**) was achieved by reduction of the C=O functional groups of the protonated polysulfonamide (**1-H**) by $LiAlH_4$ yielding the protonated polysulfonamine (**3-H**) and subsequent lithiation. Complete reduction of the polymer backbone was confirmed by solution NMR (^1H shift of the NH signal from 10.6 to 4.3 ppm, ^{13}C shift from 165.7 ppm for C=O to 46.8 ppm for CH_2, spectra of the final product are shown in the Supplemental Information, Figure S13). From the obtained polysulfonamine (**3**) (see Figure 7A), a polymer electrolyte membrane (**3b**) was fabricated similar to (**1b**), including a solvent uptake of 140 wt % (EC:PC), rendering straightforward comparison of (**1b**) and (**3b**) feasible. The introduced membrane (**3b**) affords a similar morphology as (**1b**) and has a rather dense macroscopic structure without micrometer-sized pores (Figure 7E), as anticipated from the polarity of the polymer compounds and solvents (cf. as discussed in the beginning of this section). On the nanometer scale (SAXS analysis, Figure 7F), particularly the q^{-4} dependence and peak at 0.16 nm^{-1} reveal phase separation with 39.25 nm distance between crystalline PVdF-HFP domains (which is roughly twice as in (**1b**)). In case of (**3b**), an impressive increase of ionic conductivity was observed within the considered temperature range (250–350 K, Figure 7D), although the Li^+ ion self-diffusivity of both materials (derived from PFG NMR) remained almost constant after modification of the polymer backbones ((**1b**): $D_{Li^+} = 4.6 \cdot 10^{-11} \pm 0.2\ m^2s^{-1}$; (**3b**): $4.7 \cdot 10^{-11} \pm 0.2 m^2s^{-1}$, each at 20°C). The latter observation is not consistent with the MD data (where the increase of self-diffusion coefficients and ionic conductivity for (**3b**) were similar), hence suggesting that the achieved increase in ionic conductivity is due to higher concentrations of free Li^+ ions, e.g., the ones not associated with a polymer backbone. However, in order for this mechanism to be fully valid, the average residence times of Li^+ ions at polymer sites should be longer than effective observation/correlation times typically sampled in PFG NMR measurements. In addition, the Li^+ transference number of (**3b**) was determined to be $t_{Li^+} = 0.9$ (Figure 8A), identical to the value obtained for precursor material (**1b**) (Borzutzki et al., 2019), as anticipated, since the invoked modification of the backbone should not alter the anionic (polymer backbone) mobility. Based on the determined transport properties, the ion mobility and degree of ion dissociation in case (**3b**) is estimated by applying the Einstein relation and Nernst-Einstein equation (Supplemental Information, Equations S15 and S16) (Borzutzki et al., 2019), revealing that the backbone modification results in higher fractions of dissociated Li^+ ions (45% ± 4% (**3b**) rather than 29% ± 4% (**1b**)), in good agreement with predictions from MD simulations. Note that the comparison of polymer segmental dynamical relaxations for both (**1b**) and (**3b**) disclosed almost identical incoherent dynamical structural factors, therefore indicating that the change in Li^+ dissociation with the polymeric anion is the primary cause for enhanced transport instead of enhanced flexibility of polymer chains. Since the repeat unit of single ion conducting polymer chains within the MD simulation remained constant at x = 16, an apparent change in molecular weight can be safely excluded as potential origin for the achieved improvement of the ionic conductivity for (**3b**). Rather, better tortuosity within (**3b**), as reflected by increased

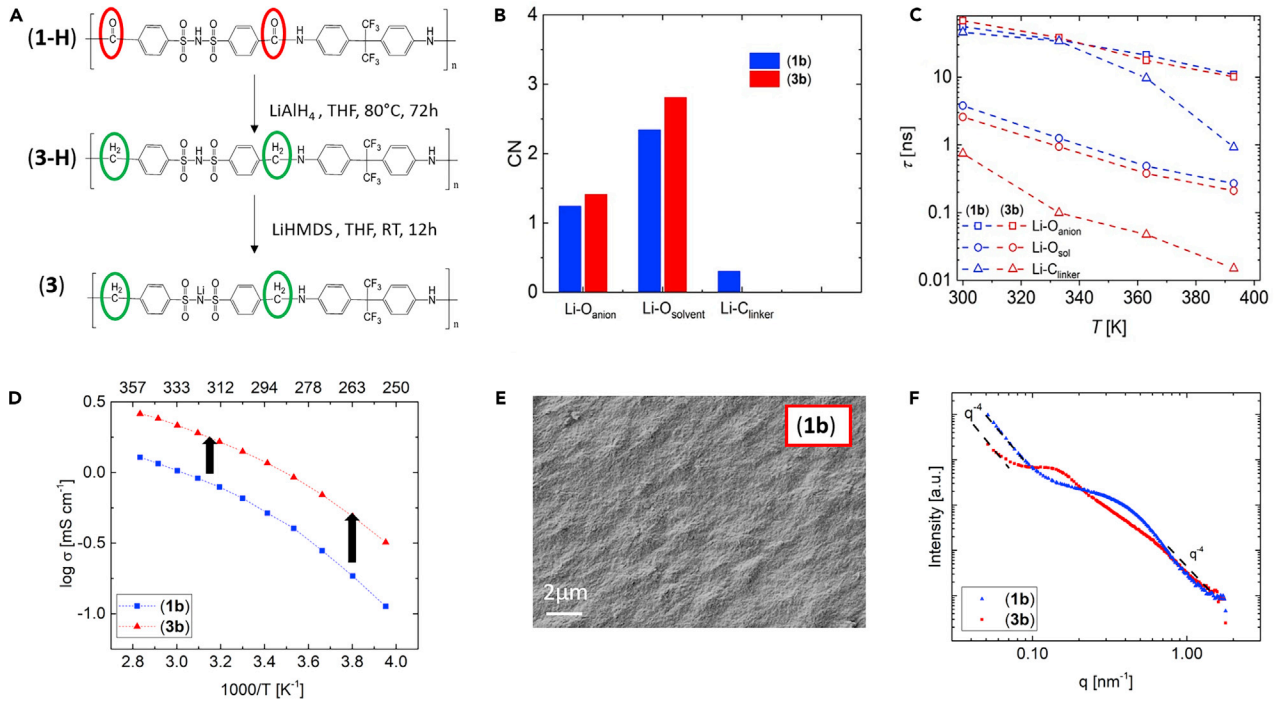

Figure 7. Chemical Modification of (1) and Characterization of the Subsequent Compound (3) and Membrane (3b)

(A) Synthesis route and chemical structures of fluorinated polysulfonamine (**3**), as modification of (**1**); (B) Comparison of MD data for Li^+ coordination numbers with anion, solvent, and linker in (**1b**) and (**3b**) (the C_{linker} is the linker carbon that bonds to N in original amide groups, highlighted with red circle in (A), whereas the Li^+-C_{linker} RDF can be found in Figure S6); (C) Residence times of Li^+ inside the first coordination shell of different groups obtained from MD simulations of (**1b**) and (**3b**); (D) Experimental temperature-dependent ionic conductivity of (**1b**) and (**3b**); (E) SEM image of (**3b**); and (F) SAXS data for (**1b**) and (**3b**).

distances between crystalline PVdF-HFP domains and hence localized changes of the channel structure, facilitates more effective transport of Li^+ ions in (**3b**) compared with (**1b**), although the concept of tortuosity in practice is not always consistently defined (Ghanbarian et al., 2013).

The electrochemical stability window of (**3b**) determined by linear sweep voltammetry is shown in Figure 8B. In the oxidative curve (red), an increase in current density at potentials higher than 4.6 V versus Li|Li^+ reveals decomposition of the polymer membrane, whereas in the reductive part (black), a slight increase in current density occurs at potentials below 1.0 V versus Li|Li^+ reflecting ongoing reduction of ethylene carbonate (Zhang et al., 2002; Nguyen et al., 2018); at a potential of 0 V versus Li|Li^+, plating of metallic Li occurs.

Long-term cycling stability of the introduced polyamine blend (**3b**) against Li metal was demonstrated by stripping/plating experiments at a current density of 0.1 mA cm^{-2} for 1 h per half cycle (Figure 9B). The voltage profiles exhibit an almost rectangular shape, evidencing that no detrimental polarization effects occurred. The overvoltage slightly decreases from 25 to 20 mV within 250 h, reflecting a slight roughening of Li metal electrode surfaces upon continuous deposition/dissolution of lithium, although the absence of significant changes in the progression of the overvoltage confirm long-term stability of (**3b**) against Li metal. The rate performance and long-term stability in LFP-based cells at 60°C is also demonstrated (Figures 9C and 9D). Note that the operational temperature was set to T = 60°C in all cycling investigations, in this way allowing for representative electrochemical performance. As demonstrated in Figure 9A, as the operational temperature is set to T = 20°C, the electrolyte resistance R_{EL} of the cell increases by less than a factor of two (from 4.2 ± 1.2 to 7.7 ± 1.2 Ω), in agreement to the values obtained for ionic conductivity, whereas the interphase resistance $R_{SEI/CEI}$ (of both cathode and anode interface) and the accumulated charge transfer resistance R_{CT} of both electrodes are increased by a factor of 3 (24.9 ± 0.4 versus 74.1 ± 0.6 Ω) and 13 (145.1 ± 3.0 versus 1,904.9 ± 172.0 Ω), respectively. This clearly indicates that electrode interphases and charge transfer kinetics are the limiting factors during cell operation, which result in a larger voltage drop; thus, the cutoff voltage is being reached at a lower cathode potential, which in turn

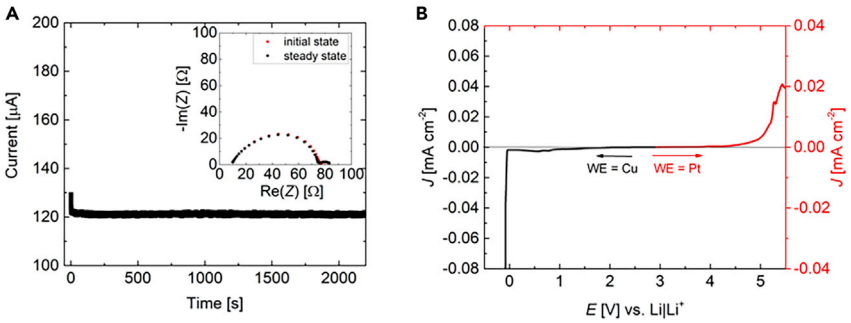

Figure 8. Determination of the Transference Number of (3b)
(A) Chronoamperometry and impedance measurement; (B) Electrochemical stability window.

yields a significant decrease in achievable specific capacity while capacity decay is reduced, as also reported for other comparable polymer electrolytes (Qin et al., 2015; Pan et al., 2016; Borzutzki et al., 2019; Li et al., 2019).

The specific capacity obtained at a moderate discharge rate of 0.05 C amounts to 150.5 $mAhg^{-1}$, whereas at faster discharge rates specific capacities of 139.5 (1C) and 93.6 $mAhg^{-1}$ (2C) can be achieved. Long-term cycling was performed at charge/discharge rates of 0.5C at which a specific capacity of 142.8 $mAhg^{-1}$ is reached in the first cycle. The Coulombic efficiency in every cycle is >99.7%, and after 70 cycles, 98.8% of the initial specific capacity (141.1 $mAhg^{-1}$) is still retained demonstrating the excellent longevity of the blend polymer membrane. Figure 9E shows the specific capacity and Coulombic efficiency of NMC111||Li cells for (**2b**) and (**3b**), respectively. The cells show a low Coulombic efficiency for the first cycle, which is a typical behavior observed in NMC-based batteries and can be attributed to structural or kinetic changes within the cell (Choi and Manthiram, 2005; Kang et al., 2008; Meister et al., 2016; Kasnatscheew et al., 2017). Later cycles have high Coulombic efficiency of >98.5% and specific capacity of 159.4 $mAhg^{-1}$ at C/20 and 148.3 $mAhg^{-1}$ in cycle 4 at C/10, clearly demonstrating the suitability and high potential of the introduced polymer electrolyte for application in LMBs (and possibly also LIBs). Note, though, that in polymer electrolyte-based LIBs or LMBs, insufficient stability of (internal) interfaces constitutes a major issue with respect to potential long-term application and longevity of cells (Bouchet et al., 2013; Cai et al., 2014a, 2014b; Cheng et al., 2018). Compared with their liquid counterpart, polymer electrolytes cannot readily penetrate porous cathodes, often yielding higher interfacial resistances that impair fast charging/discharging procedures (Bouchet et al., 2013; Cai et al., 2014a, 2014b). Considering the development of high-performance but affordable polymer structures with excellent charge carrier transport properties, tailored design of electrode/electrolyte interfaces and interphases based on strategies derived from MD simulations, including detailed understanding of charge carrier transport dynamics and structural features, indeed constitutes a valid way toward future industrial application of invented polymer electrolytes (Cai et al., 2014a, 2014b; Zeng et al., 2018), as successfully demonstrated by the current case study of quasi-solid blend polymer electrolytes. Indeed, combining computational and experimental data, it is proposed that likely Li^+ traps comprising chemical moieties that potentially could strongly bind to Li^+ ion (such as, e.g., double-bonded oxygen atoms within the polymer backbone or side chains) should be avoided, particularly involving double-bonded oxygen atoms (such as C=O or SO_2 groups reflecting highly prominent units present in many recently reported polymer structures) (Zhang et al., 2014a, 2014b; Pan et al., 2015; Nguyen et al., 2018; Zhang et al., 2018; Li et al., 2018). This concept is applicable to anionic moieties, which for future polymer designs could be chosen/modified such that (besides increasing charge delocalization as strategy for single ion polymer designs [Zhang et al., 2017a, 2017b]) no strongly ion-binding functional groups remain at either the backbone or side chains. Unlike previous design strategies of quasi-solid or even gel-type electrolytes, which mainly focused on increasing plasticizer/solvent contents for an enhanced porosity of polymer membranes, all functional groups available in the material should be evaluated with respect to their impact on the achievable bulk properties of the electrolytes, including charge carrier dynamics.

Conclusion

In this work, a holistic concept for materials development is proposed that delivers systematic improvement of polymer electrolytes based on detailed understanding of charge carrier transport dynamics

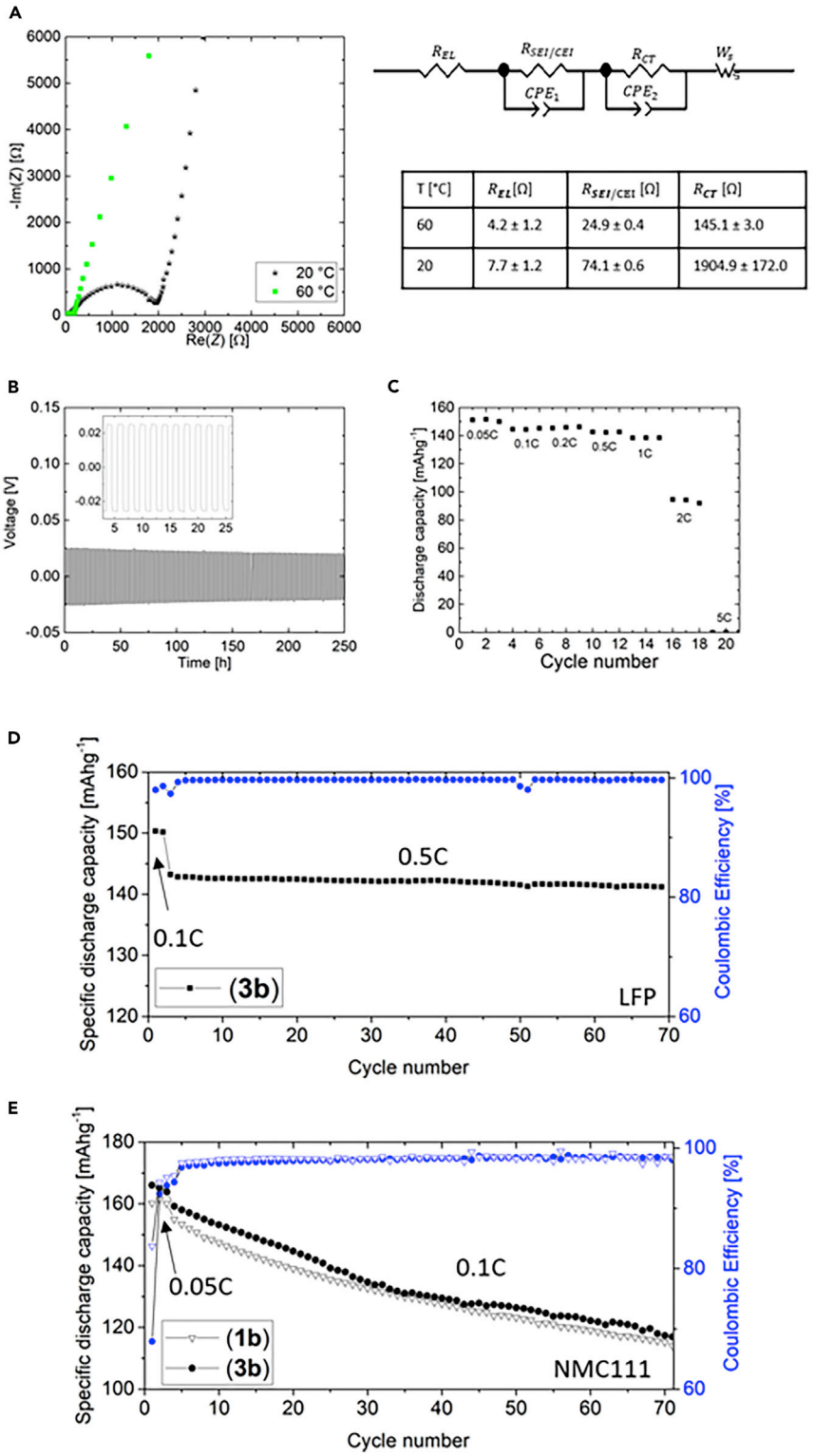

T [°C]	R_{EL} [Ω]	$R_{SEI/CEI}$ [Ω]	R_{CT} [Ω]
60	4.2 ± 1.2	24.9 ± 0.4	145.1 ± 3.0
20	7.7 ± 1.2	74.1 ± 0.6	1904.9 ± 172.0

Figure 9. Electrochemical Characterization of (3b)

(A) EIS spectra and corresponding resistances of (**3b**) assembled in an NMC||Li cell at 20°C and 60°C; (B) Voltage versus time curves for a symmetrical Li||Li cell cycled at 0.1 mA/cm^2 at 60°C for 1 h per half cycle; (C–E) Galvanostatic cycling at 60°C: (C) Rate performance test of (**3b**) in a Li||LFP cell, (D) Long-term cycling of (**3b**) in a Li||LFP cell, and (E) Comparison of the long-term performance of (**3b**) and (**2b**) in an NMC111||Li cell.

and structural features from combined computational and experimental data, and in principle is also applicable for prediction of polymer processing strategies at interfaces. It is emphasized that apparently negligible variations in polymer architectures can have significant impact on the achievable bulk materials properties such as morphology (structural features) or ion transport properties (charge carrier dynamics). The concept is successfully demonstrated on single-ion conducting polysulfonamide polymer blends, where an exchange of sulfonyl (SO_2) moieties with $C(CF_3)_2$ units within the polymer backbone not only alters the macroscopic morphology from porous to homogeneous structures but also boosts the available charge carrier transport by releasing previously bound Li^+ ions (whose residence times revealed long-lived binding with available double-bonded oxygen atoms). Hence, as general design strategy, strong polar groups or strongly coordinating anions of the backbone (or side chains) of the polymer that impair effective Li^+ ion mobility should be replaced, as evidenced by modification of a polyamide polymer architecture to a polyamine backbone, affording an enhanced room temperature ionic conductivity of 1.2 mS cm^{-1}, which is the highest value among comparable quasi-solid polymer electrolytes (with respect to plasticizer/solvent contents) reported so far, clearly reflecting a higher degree of ion dissociation, as predicted by MD simulations. In addition, excellent electrochemical performance, such as oxidative stability to potentials of up to 4.6 V versus $Li|Li^+$, stability against Li metal, and long-term cycling in NMC111||Li cells were achieved for the introduced polymer electrolyte (**3b**), illustrating the applicability of the proposed concept for advancement and design of single-ion conducting polymer electrolytes suitable for application in lithium ion and Li-metal batteries, and also other cases of energy storage and conversion including fuel cells, or electromechanical actuators as well as separation membranes.

Limitations of the Study

For the current study, the thickness of the polymer membranes was around 80 μm, which is comparably thick considering conventional separators in case of liquid electrolyte-based LIBs (e.g., 25 μm for a Celgard 2,500 separator). Although significantly thinner membranes of 40 μm thickness were successfully fabricated within the frame of the study, processing (including punching and cell assembly) becomes more challenging with decreasing sample thickness since handling of the highly flexible membranes can readily result in membrane damage. However, reduction of membrane thickness is indeed required to achieve polymer-based LMBs that are competitive to current state-of-the-art liquid electrolyte-based cells (in terms of costs/volume/mass) as well as to reduce electrolyte and interface resistances. Thus, further optimization of membrane processing steps are highly desired.

Beyond that, in the present study, the applicability of the analyzed polymers was demonstrated by galvanostatic cycling under mild conditions (low current densities and elevated temperature), whereas for most real-life applications fast charging/discharging procedures at room temperatures are required.

Resource Availability

Lead Contact

Further information and requests for resources may be addressed to one of the Lead Contacts: Gunther Brunklaus: g.brunklaus@fz-juelich.de Kristina Borzutzki: k.borzutzki@fz-juelich.de.

Materials Availability

Additional information is available from the Lead Contact upon reasonable request.

Data and Code Availability

All data and additional information are available from the Lead Contact upon reasonable request.

METHODS

All methods can be found in the accompanying Transparent Methods supplemental file.

SUPPLEMENTAL INFORMATION

Supplemental Information can be found online at https://doi.org/10.1016/j.isci.2020.101417.

ACKNOWLEDGMENTS

D.D. and D.B. gratefully acknowledge support from the project sponsored by the Army Research Laboratory, United States under Cooperative Agreement Number W911NF-12-2-0023. The views and conclusions contained in this document are those of the authors and should not be interpreted as representing the official policies, either expressed or implied, of ARL or the US Government. The US Government is authorized to reproduce and distribute reprints for Government purposes not withstanding any copyright notation herein. We would also like to acknowledge the Center of High Performance Computing at the University of Utah for generous allocation of computation. The authors K.B., M.W., and G.B. gratefully acknowledge generous support provided by the German Federal Ministry of Education and Research (BMBF) projects "Festbatt" (grant 13XP0175A) and "Benchbatt" (03XP0047B). Special thanks also to Constantin Lürenbaum for TXRF measurements, Marcel Diehl for ICP-OES measurements, as well as Uta Rodehorst and Jens Wrogemann for the XRD measurements.

AUTHOR CONTRIBUTIONS

K.B and D.D. contributed equally to this work. Concept, K.B, G.B., C.W., D.D., and D.B.; Methodology, K.B. (Synthesis, NMR, SEM, and electrochemical measurements), M.K. (SAXS), and A.S. (AFM); MD simulations D.D. and D.B.; Writing – Original Draft, K.B. and D.D.; Writing – Review & Editing, G.B., D.B., and M.W.; Supervision, G.B., D.B., and M.W.

DECLARATION OF INTERESTS

The authors declare no competing financial interests.

Received: May 18, 2020
Revised: July 7, 2020
Accepted: July 24, 2020
Published: August 21, 2020

REFERENCES

Allen, J.L., Borodin, O., Seo, D.M., and Henderson, W.A. (2014). Combined quantum chemical/Raman spectroscopic analyses of Li+ cation solvation: cyclic carbonate solvents - ethylene carbonate and propylene carbonate. J. Power Sources *267*, 821–830.

Bedrov, D., Pequemal, J.-P., Borodin, O., MacKerell, J.A.D., Roux, B., and Schroeder, C. (2019). Polarizable molecular dynamics simulations of ionic and polar systems. Chem. Rev. *119*, 7940–7995.

Bedrov, D., Piquemal, J.-P., Borodin, O., Mackerell, A.D., and Schröder, C. (2018). Molecular dynamics simulations of ionic liquids and electrolytes using polarizable force fields. Chem. Rev. *119*, 7940–7995.

Borodin, O., and Smith, G.D. (2006a). Mechanism of ion transport in amorphous poly(ethylene oxide)/LiTFSI from molecular dynamics simulations. Macromolecules *39*, 1620–1629.

Borodin, O., and Smith, G.D. (2006b). LiTFSI structure and transport in ethylene carbonate from molecular dynamics simulations. J. Phys. Chem. B *110*, 4971–4977.

Borzutzki, K., Thienenkamp, J., Diehl, M., Winter, M., and Brunklaus, G. (2019). Fluorinated polysulfonamide based single ion conducting room temperature applicable gel-type polymer electrolytes for lithium ion batteries. J. Mater. Chem. A *7*, 188–201.

Bouchet, R., Maria, S., Meziane, R., Aboulaich, A., Lienafa, L., Bonnet, J.P., Phan, T.N.T., Bertin, D., Gigmes, D., Devaux, D., et al. (2013). Single-ion BAB triblock copolymers as highly efficient electrolytes for lithium-metal batteries. Nat. Mater. *12*, 452–457.

Cai, W., Li, J., Zhang, Y., Xu, G., Rohan, R., Sun, Y., and Cheng, H. (2014a). Current status and future prospects of research on single ion polymer electrolyte for lithium battery applications. J. Chin. Ceram. Soc. *1*, 78–92.

Cai, W., Zhang, Y., Li, J., Sun, Y., and Cheng, H. (2014b). Single-ion polymer electrolyte membranes enable lithium-ion batteries with a broad operating temperature range. ChemSusChem *7*, 1063–1067.

Chazalviel, J.-N. (1990). Electrochemical aspects of the generation of ramified metallic electrodeposits. Phys. Rev. A *42*, 7355–7367.

Chen, N., Yao, X., Zheng, C., Tang, Y., Ren, M., Ren, Y., Guo, M., Zhang, S., and Liu, L.Z. (2017a). Study on the miscibility, crystallization and crystalline morphology of polyamide-6/polyvinylidene fluoride blends. Polymer *124*, 30–40.

Chen, Y., Li, Z., Liu, X., Zeng, D., Zhang, Y., Sun, Y., Ke, H., and Cheng, H. (2017b). Construction of interconnected micropores in poly(arylene ether) based single ion conducting blend polymer membranes via vapor-induced phase separation. J. Membr. Sci. *544*, 47–57.

Chen, Y., Xu, G., Liu, X., Pan, Q., Zhang, Y., Zeng, D., Sun, Y., Ke, H., and Cheng, H. (2018). A gel single ion conducting polymer electrolyte enables durable and safe lithium ion batteries via graft polymerization. RSC Adv. *8*, 39967–39975.

Cheng, X., Pan, J., Zhao, Y., Liao, M., and Peng, H. (2018). Gel polymer electrolytes for electrochemical energy storage. Adv. Energy Mater. *8*, 1702184.

Choi, J., and Manthiram, A. (2005). Investigation of the irreversible capacity loss in the layered LiNi1/3Mn1/3Co1/3O2 cathodes. Electrochem. Solid State Lett. *8*, C102–C105.

Cornet, N., Diat, O., Gebel, G., Jousse, F., Marsacq, D., Mercier, R., and Pineri, M. (2000). Sulfonated polyimide membranes: a new type of ion-conducting membrane for electrochemical applications. J. New Mater. Electrochem. Syst. *3*, 33–42.

Deng, K., Wang, S., Ren, S., Han, D., Xiao, M., and Meng, Y. (2017). Network type sp3 boron-based single-ion conducting polymer electrolytes for lithium ion batteries. J. Power Sources *360*, 98–105.

Deng, K., Zeng, Q., Wang, D., Liu, Z., Qiu, Z., Zhang, Y., Xiao, M., and Meng, Y. (2020). Single-ion conducting gel polymer electrolytes: design, preparation and application. J. Mater. Chem. *8*, 1557–1577.

Dong, J., Zhang, Y., Wang, J., Yang, Z., Sun, Y., Zeng, D., Liu, Z., and Cheng, H. (2018). Highly

porous single ion conducting polymer electrolyte for advanced lithium-ion batteries via facile water-induced phase separation process. J. Membr. Sci. *568*, 22–29.

Franco, A.A., Rucci, A., Brandell, D., Frayret, C., Gaberscek, M., Jankowski, P., and Johansson, P. (2019). Boosting rechargeable batteries R&D by multiscale modeling: myth or reality? Chem. Rev. *119*, 4569–4627, review-article.

Ganesan, V., and Jayaraman, A. (2014). Theory and simulation studies of effective interactions, phase behavior and morphology in polymer nanocomposites. Soft Matter. *10*, 13–38.

Gao, Q., and Scheinbeim, J.I. (2000). Dipolar intermolecular interactions, structural development, and electromechanical properties in ferroelectric polymer blends of nylon-11 and poly(vinylidene fluoride). Macromolecules *33*, 7564–7572.

Gartner, T.E., and Jayaraman, A. (2019). Modeling and simulations of polymers: a roadmap. Macromolecules. Am. Chem. Soc. *52*, 755–786.

Ghanbarian, B., Hunt, A.G., Ewing, R.P., and Sahimi, M. (2013). Tortuosity in porous media: a critical review. Soil Sci. Soc. Am. J. *77*, 1461–1477.

Hammouda, B. (2008). Probing Nanoscale Structures (National Institute of Standards and Technology).

Janek, J., and Zeier, W.G. (2016). A solid future for battery development. Nat. Energy *1*, 1–4.

Jia, H., Onishi, H., von Aspern, N., Rodehorst, U., Rudolf, K., Billmann, B., Wagner, R., Winter, M., and Cekic-Laskovic, I. (2018a). A propylene carbonate based gel polymer electrolyte for extended cycle life and improved safety performance of lithium ion batteries. J. Power Sources *397*, 343–351.

Jia, H., Onishi, H., Wagner, R., Winter, M., and Cekic-Laskovic, I. (2018b). Intrinsically safe gel polymer electrolyte comprising flame-retarding polymer matrix for lithium ion battery application. ACS Appl. Mater. Interfaces *10*, 42348–42355.

Kang, S.H., Yoon, W.S., Nam, K.W., Yang, X.Q., and Abraham, D.P. (2008). Investigating the first-cycle irreversibility of lithium metal oxide cathodes for Li batteries. J. Mater. Sci. *43*, 4701–4706.

Kasnatscheew, J., Evertz, M., Streipert, B., Wagner, R., Nowak, S., Laskovic, I.C., and Winter, M. (2017). Changing established belief on capacity fade mechanisms: thorough investigation of LiNi1/3Co1/3Mn1/3O2(NCM111) under high voltage conditions. J. Phys. Chem. C *121*, 1521–1529.

Kesting, R.E. (1990). The four tiers of structure in integrally skinned phase inversion membranes and their relevance to the various separation regimes. J. Appl. Polym. Sci. *41*, 2739–2752.

Ketkar, P.M., Shen, K.H., Hall, L.M., and Epps, T.H. (2019). Charging toward improved lithium-ion polymer electrolytes: exploiting synergistic experimental and computational approaches to facilitate materials design. Mol. Syst. Des. Eng. *4*, 223–238.

Lagadec, M.F., Zahn, R., and Wood, V. (2019). Characterization and performance evaluation of lithium-ion battery separators. Nat. Energy *4*, 16–25.

Li, C., Qin, B., Zhang, Y., Varzi, A., Passerini, S., Wang, J., Dong, J., Zeng, D., Liu, Z., and Cheng, H. (2019). Single-ion conducting electrolyte based on electrospun nanofibers for high-performance lithium batteries. Adv. Energy Mater. *9*, 1–9.

Li, Z., Lu, W., Zhang, N., Pan, Q., Chen, Y., Xu, G., Zeng, D., Zhang, Y., Cai, W., Yang, M., et al. (2018). Single ion conducting lithium sulfur polymer batteries with improved safety and stability. J. Mater. Chem. A *6*, 14330–14338.

Liu, Y., Zhang, Y., Pan, M., Liu, X., Li, C., Sun, Y., Zeng, D., and Cheng, H. (2016). A mechanically robust porous single ion conducting electrolyte membrane fabricated via self-assembly. J. Membr. Sci. *507*, 99–106.

Long, L., Wang, S., Xiao, M., and Meng, Y. (2016). Polymer electrolytes for lithium polymer batteries. J. Mater. Chem. A *4*, 10038–10039.

Ma, Q., Zhang, H., Zhou, C., Zheng, L., Cheng, P., Nie, J., Feng, W., Hu, Y.-S.S., Li, H., Huang, X., et al. (2016). Single lithium-ion conducting polymer electrolytes based on a super-delocalized polyanion. Angew. Chem. Int. Ed. *128*, 2521–2525.

McGrath, J.E., Kim, Y.S., Hickner, M., Wang, F., and Zawodzinski, T.A. (2002). Direct polymerization of sulfonated poly(arylene ether sulfone) random (statistical) copolymers: candidates for new proton exchange membranes. J. Membr. Sci. *197*, 231–242.

Meister, P., Jia, H., Li, J., Kloepsch, R., Winter, M., and Placke, T. (2016). Best practice: performance and cost evaluation of lithium ion battery active materials with special emphasis on energy efficiency. Chem. Mater. *28*, 7203–7217.

Meziane, R., Bonnet, J.P., Courty, M., Djellab, K., and Armand, M. (2011). Single-ion polymer electrolytes based on a delocalized polyanion for lithium batteries. Electrochim. Acta *57*, 14–19.

Mogurampelly, S., Borodin, O., and Ganesan, V. (2016). Computer simulations of ion transport in polymer electrolyte membranes. Annu. Rev. Chem. Biomol. Eng. *7*, 349–371.

Ngai, K.S., Ramesh, S., Ramesh, K., and Juan, J.C. (2016). A review of polymer electrolytes: fundamental, approaches and applications. Ionics *22*, 1259–1279.

Nguyen, H.-D., Kim, G.-T., Shi, J., Paillard, E., Judenstein, P., Lyonnard, S., Bresser, D., and Iojoiu, C. (2018). Nanostructured multi-block copolymer single-ion conductors for safer high-performance lithium batteries. Energy Environ. Sci. *11*, 3298–3309.

Oh, H., Xu, K., Yoo, H.D., Kim, D.S., Chanthad, C., Yang, G., Jin, J., Ayhan, I.A., Oh, S.M., and Wang, Q. (2016). Poly(arylene ether)-based single-ion conductors for lithium-ion batteries. Chem. Mater. *28*, 188–196.

Oikonomou, E.K., Tencé-Girault, S., Gérard, P., and Norvez, S. (2015). Swelling of semi-crystalline PVDF by a PMMA-based nanostructured diblock copolymer: morphology and mechanical properties. Polymer *76*, 89–97.

Onorato, J.W., and Luscombe, C.K. (2019). Morphological effects on polymeric mixed ionic/electronic conductors. Mol. Syst. Des. Eng. *4*, 310–324.

Pan, Q., Chen, Y., Zhang, Y., Zeng, D., Sun, Y., and Cheng, H. (2016). A dense transparent polymeric single ion conductor for lithium ion batteries with remarkable long-term stability. J. Power Sources *336*, 75–82.

Pan, Q., Zhang, W., Pan, M., Zhang, B., Zeng, D., Sun, Y., and Cheng, H. (2015). Construction of a lithium ion transport network in cathode with lithiated bis(benzene sulfonyl)imide based single ion polymer ionomers. J. Power Sources *283*, 279–288.

Placke, T., Kloepsch, R., Dühnen, S., and Winter, M. (2017). Lithium ion, lithium metal, and alternative rechargeable battery technologies: the odyssey for high energy density. J. Solid State Electrochem. *21*, 1939–1964.

Qin, B., Liu, Z., Zheng, J., Hu, P., Ding, G., Zhang, C., Zhao, J., Kong, D., and Cui, G. (2015). Single-ion dominantly conducting polyborates towards high performance electrolytes in lithium batteries. J. Mater. Chem. A *3*, 7773–7779.

Rohan, R., Pareek, K., Cai, W., Zhang, Y., Xu, G., Chen, Z., Gao, Z., Dan, Z., and Cheng, H. (2015). Melamine-terephthalaldehyde-lithium complex: a porous organic network based single ion electrolyte for lithium ion batteries. J. Mater. Chem. A *3*, 5132–5139.

Rohan, R., Sun, Y., Cai, W., Pareek, K., Zhang, Y., Xu, G., and Cheng, H. (2014). Functionalized meso/macro-porous single ion polymeric electrolyte for applications in lithium ion batteries. J. Mater. Chem. A *2*, 2960–2967.

Sadoway, D.R., Huang, B., Trapa, P.E., Soo, P.P., Bannerjee, P., and Mayes, A.M. (2001). Self-doped block copolymer electrolytes for solid-state, rechargeable lithium batteries. J. Power Sources *97–98*, 621–623.

Schmuch, R., Wagner, R., Hörpel, G., Placke, T., and Winter, M. (2018). Performance and cost of materials for lithium-based rechargeable automotive batteries. Nat. Energy *3*, 267–278.

Shin, D.W., Guiver, M.D., and Lee, Y.M. (2017). Hydrocarbon-based polymer electrolyte membranes: importance of morphology on ion transport and membrane stability. Chem. Rev. *117*, 4759–4805.

Song, J.Y., Wang, Y.Y., and Wan, C.C. (1999). Review of gel-type polymer electrolytes for lithium-ion batteries. J. Power Sources *77*, 183–197.

Steinmüller, B., Müller, M., Hambrecht, K.R., Smith, G.D., and Bedrov, D. (2012). Properties of random block copolymer morphologies: molecular dynamics and single-chain-in-mean-field simulations. Macromolecules *45*, 1107–1117.

Sun, Y., Rohan, R., Cai, W., Wan, X., Pareek, K., Lin, A., Yunfeng, Z., and Cheng, H. (2014). A polyamide single-ion electrolyte membrane for application in lithium-ion batteries. Energy Technol. *2*, 698–704.

Trapa, P.E., Huang, B., Won, Y.Y., Sadoway, D.R., and Mayes, A.M. (2002). Block copolymer electrolytes synthesized by atom transfer radical polymerization for solid-state, thin-film lithium batteries. Electrochem. Solid State Lett. *5*, 85–88.

Van Schalkwijk, W., and Scrosati, B. (2002). Advances in Lithium-Ion Batteries (Kluwer Academic/Plenum Publisher).

Winter, M., Barnett, B., and Xu, K. (2018). Before Li ion batteries. Chem. Rev. *118*, 11433–11456.

Wu, H., Xu, Y., Ren, X., Liu, B., Engelhard, M.H., Ding, M.S., El-Khoury, P.Z., Zhang, L., Li, Q., Xu, K., et al. (2019). Polymer-in-"Quasi-Ionic liquid" electrolytes for high-voltage lithium metal batteries. Adv. Energy Mater. *9*, 1–10.

Yoon, L.K., and Kim, B.K. (2000). Compatibility of poly(vinylidene fluoride) (PVDF)/polyamide 12 (PA12) blends. J. Appl. Polym. Sci. *78*, 1374–1380.

Zeng, H., Ji, X., Tsai, F., Zhang, Q., Jiang, T., Li, R.K.Y., Shi, H., Luan, S., and Shi, D. (2018). Enhanced cycling performance for all-solid-state lithium ion battery with LiFePO4 composite cathode encapsulated by poly (ethylene glycol) (PEG) based polymer electrolyte. Solid State Ionics *320*, 92–99.

Zhang, H., Li, C., Eshetu, G.G., Laruelle, S., Grugeon, S., Zaghib, K., Julien, C., Mauger, A., Guyomard, D., Rojo, T., et al. (2020). From solid-solution electrodes and the rocking-chair concept to today's batteries. Angew. Chem. Int. Ed. *59*, 534–538.

Zhang, H., Li, C., Piszcz, M., Coya, E., Rojo, T., Rodriguez-Martinez, L.M., Armand, M., and Zhou, Z. (2017a). Single lithium-ion conducting solid polymer electrolytes: advances and perspectives. Chem. Soc. Rev. *46*, 797–815.

Zhang, S.S. (2018). Problem, status, and possible solutions for lithium metal anode of rechargeable batteries. ACS Appl. Energy Mater. *1*, 910–920.

Zhang, X., Kostecki, R., Richardson, T.J., Pugh, J.K., and Ross, P.N. (2002). Electrochemical and infrared studies of the reduction of organic carbonates. J. Electrochem. Soc. *148*, A1341.

Zhang, Y., Chen, Y., Liu, Y., Qin, B., Yang, Z., Sun, Y., Zeng, D., Varzi, A., Passerini, S., Liu, Z., and Cheng, H. (2018). Highly porous single-ion conductive composite polymer electrolyte for high performance Li-ion batteries. J. Power Sources *397*, 79–86.

Zhang, Y., Lim, C.A., Cai, W., Rohan, R., Xu, G., Sun, Y., and Cheng, H. (2014a). Design and synthesis of a single ion conducting block copolymer electrolyte with multifunctionality for lithium ion batteries. RSC Adv. *4*, 43857–43864.

Zhang, Y., Liu, Y., Liu, X., Li, C., Dong, J., Sun, Y., Zeng, D., Yang, Z., and Cheng, H. (2017b). Fluorene-containing cardo and fully aromatic single ion conducting polymer electrolyte for room temperature, high performance lithium ion batteries. Chem. Select *2*, 7904–7908.

Zhang, Y., Sun, Y., Cheng, H., Rohan, R., Cai, W., Xu, G., Lin, A., Sun, Y., Lin, A., and Cheng, H. (2014b). Influence of chemical microstructure of single ion polymeric electrolyte membranes on performance of lithium ion batteries. ACS Appl. Mater. Interfaces *6*, 17534–17542.

Zheng, Q., Pesko, D.M., Savoie, B.M., Timachova, K., Hasan, A.L., Smith, M.C., Miller, T.F., Coates, G.W., and Balsara, N.P. (2018). Optimizing ion transport in polyether-based electrolytes for lithium batteries. Macromolecules *51*, 2847–2858.

Zhong, Y., Zhong, L., Wang, S., Qin, J., Han, D., Ren, S., Xiao, M., Sun, L., and Meng, Y. (2019). Ultrahigh Li-ion conductive single-ion polymer electrolyte containing fluorinated polysulfonamide for quasi-solid-state Li-ion batteries. J. Mater. Chem. A *7*, 24251–24261.

Zhou, D., Tkacheva, A., Tang, X., Sun, B., Shanmukaraj, D., Li, P., Zhang, F., Armand, M., and Wang, G. (2019). Stable conversion chemistry-based lithium metal batteries enabled by hierarchical multifunctional polymer electrolytes with near-single ion conduction. Angew. Chem. Int. Ed. *58*, 6001–6006.

iScience, Volume *23*

Supplemental Information

Small Groups, Big Impact: Eliminating Li^+ Traps in Single-Ion Conducting Polymer Electrolytes

Kristina Borzutzki, Dengpan Dong, Christian Wölke, Margarita Kruteva, Annika Stellhorn, Martin Winter, Dmitry Bedrov, and Gunther Brunklaus

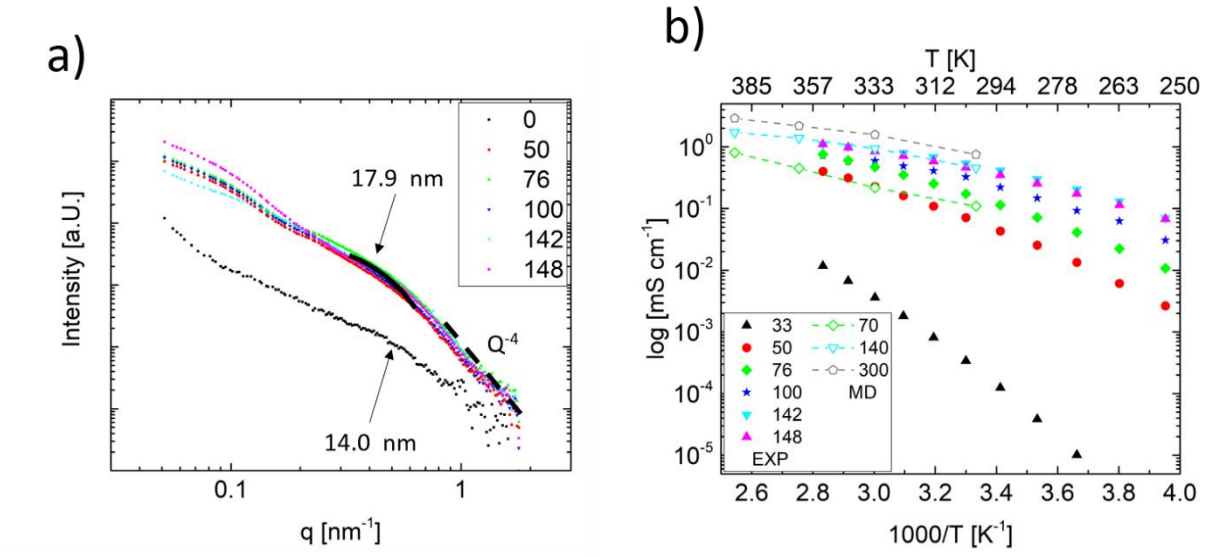

Figure S1. Influence of solvent content on membrane morphology and Li^+ transport. a) SAXS spectra, Related to Figure 2 and b) ionic conductivity, Related to Figure 5a for (**1b**) with different solvent contents (in wt%) as indicated by the numbers in the legend.

Systems of different wt% fractions were realized experimentally and their ionic conductivity as well as their morphology was determined. Figure S1 shows ionic conductivity and SAXS spectra of the systems. A reduction of the solvent content reduces the ionic conductivity of the membrane. However, a content below 50 wt% leads to a visibly incomplete wetting/inhomogeneous distribution of the solvent within the membrane explaining the drastic drop in ionic conductivity. The dry membrane (0 wt%) shows a reduction of ionic conductivity by 9 orders of magnitude. These results imply that solvent contents of < 50wt% are not feasible for cell application at practical C-rates. An increase in solvent uptake (relating to the "*natural solvent uptake*") can be achieved by heating the membrane (60 °C) while swelling. However, this increase is limited to 148 wt% as: 1) after cooling the membrane down to RT again, it releases the solvent, indicating that the natural weight uptake almost equals the maximum uptake that is possible and 2) increasing the temperature and solvent placed on the membrane even further leads to the partial dissolution of the membrane. Also note, that at an increase in EC: PC content by only 6 wt%, the membrane experiences a volume expansion.

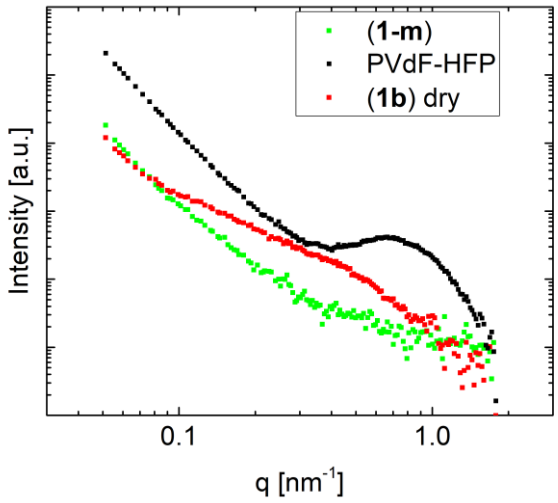

Figure S2. SAXS spectra of membranes composed of (**1**) indicated as (**1-m**), PVdF-HFP, and (**1b**) dry, Related to Figure 2.

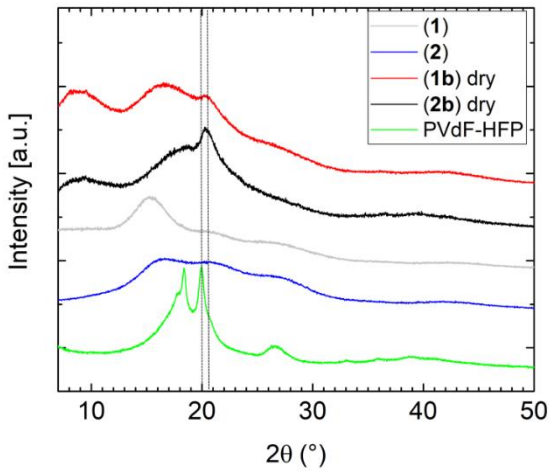

Figure S3. XRD patterns of (**1**), (**2**), PVdF-HFP and the dry membranes (**1b**) and (**2b**), Related to Figure 2.

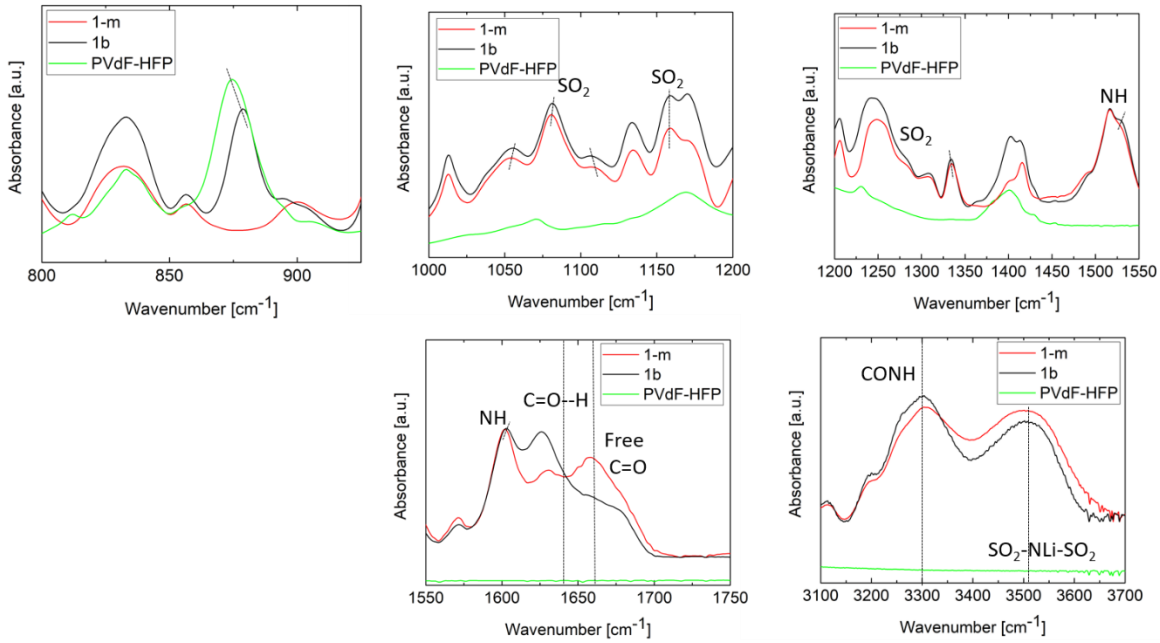

Figure S4. FTIR spectra of dry membranes composed of the single compounds (**1**) indicated as (**1-m**) and PVdF-HFP and of the dry blend membranes (**1b**), Related to Figure 2.

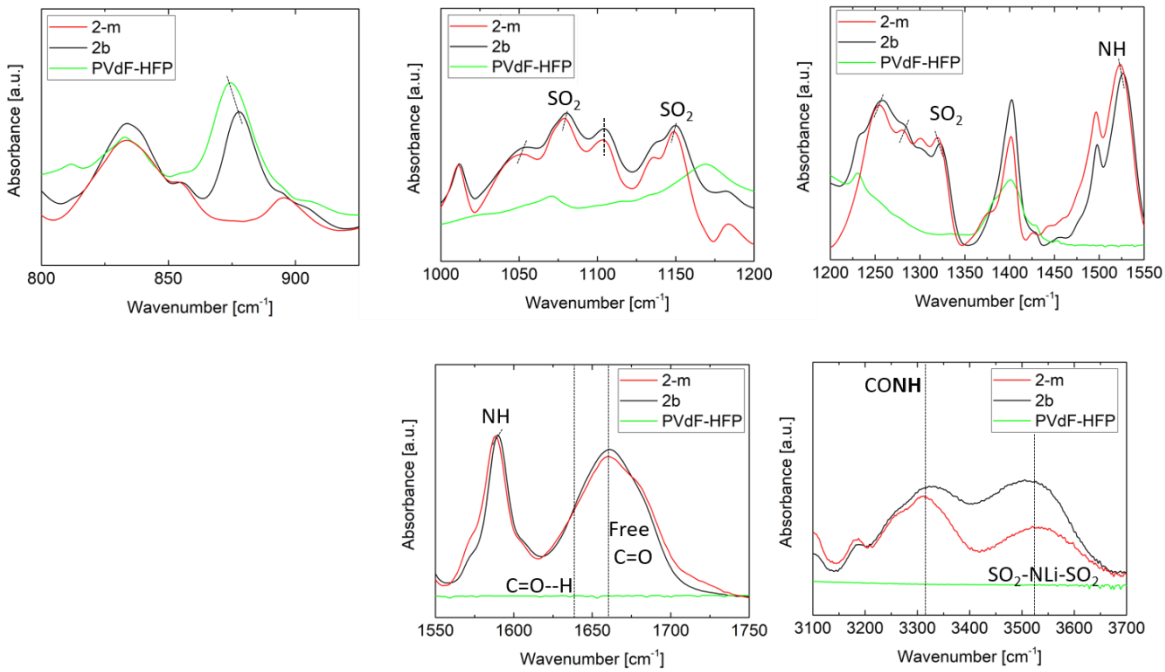

Figure S5. FTIR spectra of dry membranes composed of the single compounds (**2**) indicated as (**2-m**) and PVdF-HFP and of the dry blend membranes (**2b**), Related to Figure 2.

FTIR spectra in Figure S4 and S6 indicate interactions between (**1**) and (**2**) with PVdF-HFP in (**1b**) and (**2b**), respectively as shifts and changes in intensities of various peaks in the spectra in (**1b**) and (**2b**) compared to (**1-m**) and (**2-m**) can be observed. In previous works the interaction of Nylon and PVdF

blends was studied in detail by IR investigations of a variety of different blend compositions and the corresponding shifts of the peak positions corresponding to CH_2, CF_2, NH and CO groups were analyzed demonstrating NH—F and C=O—H interactions between the two polymers.(Gao & Scheinbeim, 2000) In our case, peaks corresponding to CH_2 and CF_2 from PVdF-HFP overlap with peaks from (**1-m**) and (**2-m**) and changes are not detectable due to the low content of 25 wt% of PVdF-HFP in the blend. However, a change in the position of the skeletal band at 870 cm^{-1} is clearly visible implying a change in the crystal structure of PVdF-HFP upon blending (in agreement to the shift of the reflection in XRD from 2θ = 20.0 in PVdF-HFP to 2θ = 20.4 in (**1b**) and (**2b**) in Figure S4). Focussing on the polyamide IR signals, in both systems the NH peaks at 1533 cm^{-1} and 1588 cm^{-1} (δN-H, secondary amide) equally shift towards higher wavenumbers upon blending. Both observations are in good agreement with studies on Nylon/ PVdF blend membranes confirming the interactions of the blend partners.(Gao & Scheinbeim, 2000)

In addition, a variety of peak shifts can be observed in the range from 1000 cm^{-1} to 1350 cm^{-1} referring to CH out of plane vibrations of 1,4-substituted benzene as well as SO_2 at 1079 cm^{-1} (symmetric stretching ν_s), 1150 cm^{-1} / 1158 cm^{-1} (antisymmetric stretching ν_a) and 1286 cm^{-1} (δ_{SO2}) for SO_2NLiSO_2.(Pan et al., 2015) Indeed, the interpretation of peak shifts in this range is difficult due to the influence of the addition of PVdF-HFP.However in both systems a shift of the SO_2 stretching at 1079 cm^{-1} towards higher wavenumbers can be observed even though PVdF-HFP signal decreases in this range (which in case of simple superposition of both spectra) would result in a shift to lower wavenumbers instead. This opposing behavior also occurs for the signal at 1107 cm^{-1} corresponding to CH in plane deformation (shifting to lower wavenumbers in (**1b**)/ no shift in (**2b**) though PVdF-HFP increases) as well as for signals between 1225 cm^{-1} and 1325 cm^{-1} in (**2-m**)/(**2b**) referred to SO_2 and CH out of plane deformations.(Socrates, 2001) In addition the signal of the additional SO_2 group of (**2b**) at 1325 cm^{-1} (absence of PVdF-HFP signals) shift towards higher wavenumbers demonstrating the existence of O—H interactions. At 1640 cm^{-1} and 1660 cm^{-1} bound and unbound C=O groups, respectively, are visible. For (**1b**), the content of bound oxygen increases significantly pointing to an

interaction with hydrogen atoms of PVdF-HFP(Gao & Scheinbeim, 2000) whereas this trend cannot be clearly identifies in (**2b**). In the range between 3300 cm^{-1} and 3600 cm^{-1} secondary amide peaks are present, whereby the broad peak at 3300 cm^{-1} belongs to the CONH coupling and the one at 3533 cm^{-1} to the sulphonamide group. It is known that the N-H stretching band shift to lower wavenumbers when the interaction between N-H and C-F in blends is stronger than N-H and C=O interaction in polyamides alone which implies that some hydrogen bonds between N-H and C=O are broken.(Gao & Scheinbeim, 2000) However, due to the strong overlap of both polyamide signals in addition to overlapping area from neighboring peaks conclusions or fitting in this area is rather ambiguous for these systems. It can be concluded, that in both systems peak shifts corresponding to SO_2, C=O, NH or CH (from 1,4 substituted benzene) indicate, that there are specific CH—F, CH—O intermolecular interactions(Thalladi et al., 1998; Smart, 2001; Mocilac, Osman, & Gallagher, 2016) (particularly stronger C=O—NH interactions in (**1b**) and preferentially SO—NH interactions in (**2b**)) and hence partly miscibility of the blend partners in (**1b**) and (**2b**).

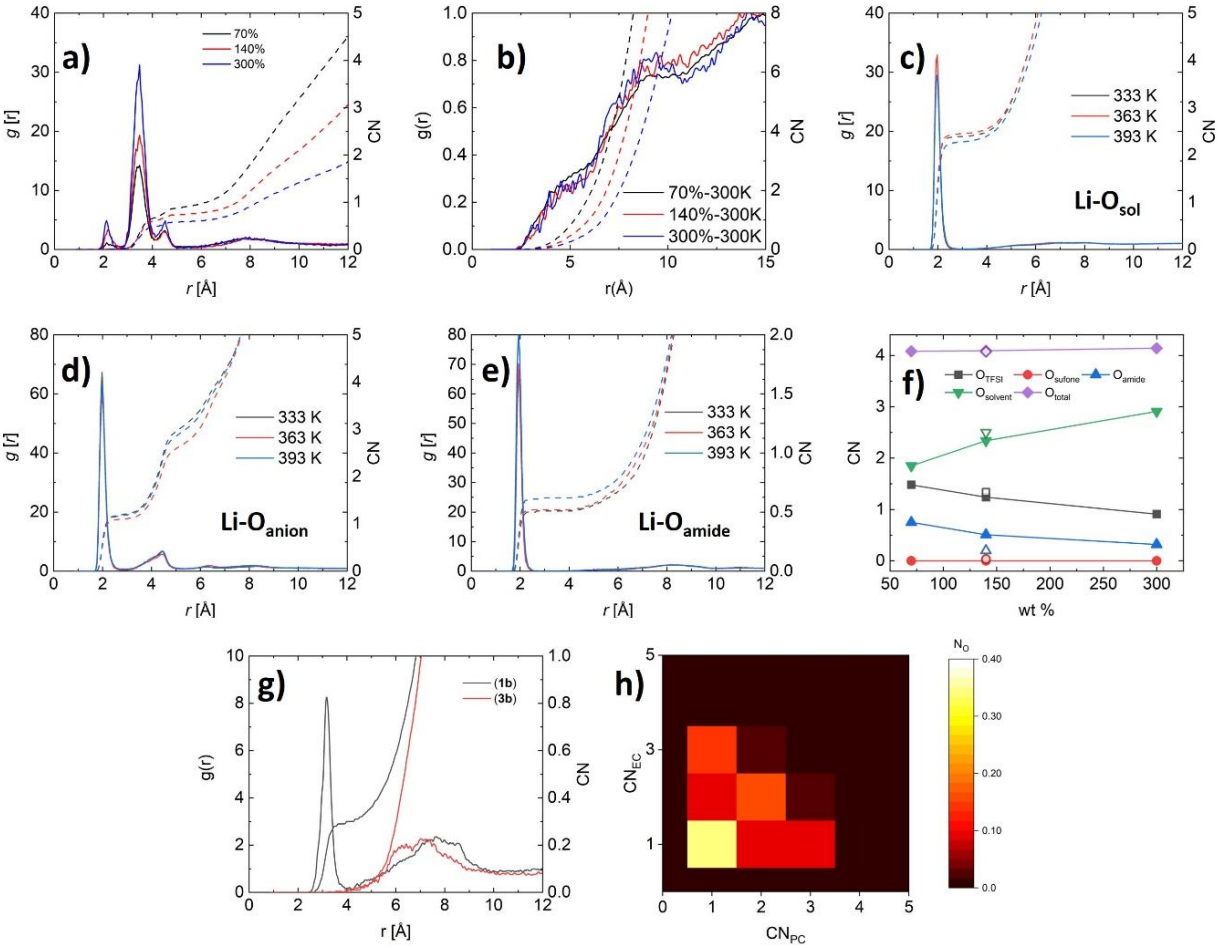

Figure S6. The coordination environment around Li^+ in **(1b)**: a) Li-N_{anion} RDF at 300 K, b) Li-F RDF at 300K, c) Li-$O_{solvent}$ RDF, d) Li-O_{anion} RDF, e) Li-O_{amide} RDF, f) coordination number within first Li-O coordination shell at different solvent content for (**1b**) and at 140 wt% for (**2b**), g) comparison of Li-C_{linker} RDF and CN between (**1b**) and (**3b**) at 300 K, and h) probability (color scale) of different solvation structures (EC versus PC molecules) of Li^+ in (**3b**), Related to Figure 5a.

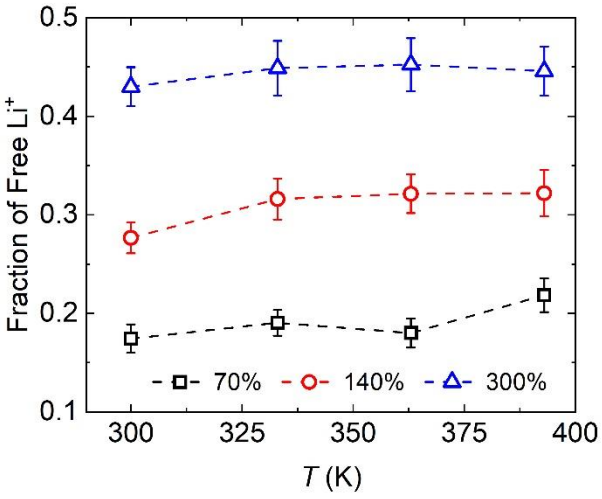

Figure S7. Fraction of Li^+ located outside first coordination shell of Li^+-O in (**1b**), Related to Figure 5.

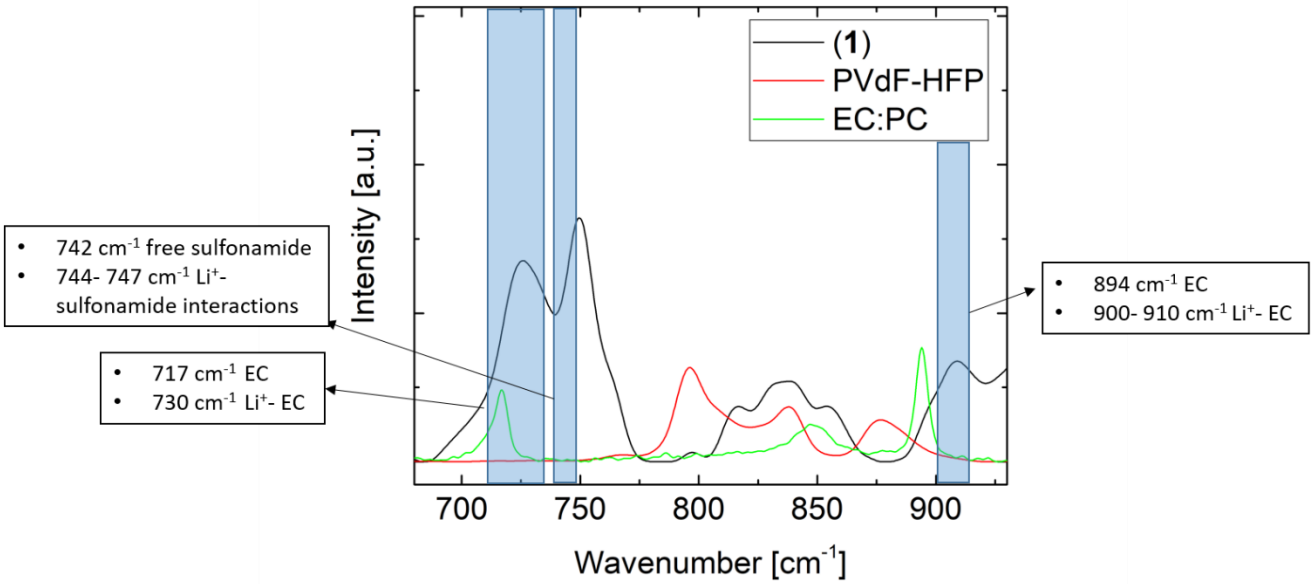

Figure S8. Raman spectra of the single compounds of the membrane. The ranges for analysis of Li^+ ion interactions/dissoziation(Morita et al., 1998; Tchitchekova et al., 2017) are highlighted indicating the overlapp of these signals with other signals arising from functional groups of the single ion conducting polymer backbone, Related to Figure 5.

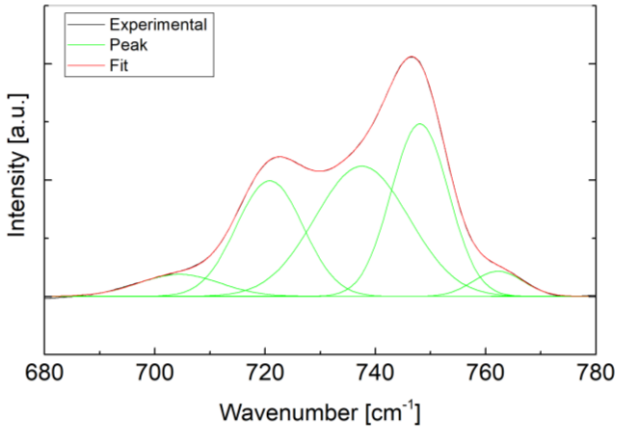

Figure S9. Fitting of the Raman spectrum of (**1**) in the range potentially revealing Li^+ ion interactions (Li^+-anion, Li^+-solvent) in the polymer membrane. The high amount of signals arising from the polymer backbone in the relevant range indicate that quantification of Li dissociation is ambiguous especially as the composition of the membrane changes between different samples analyzed, Related to Figure 5.

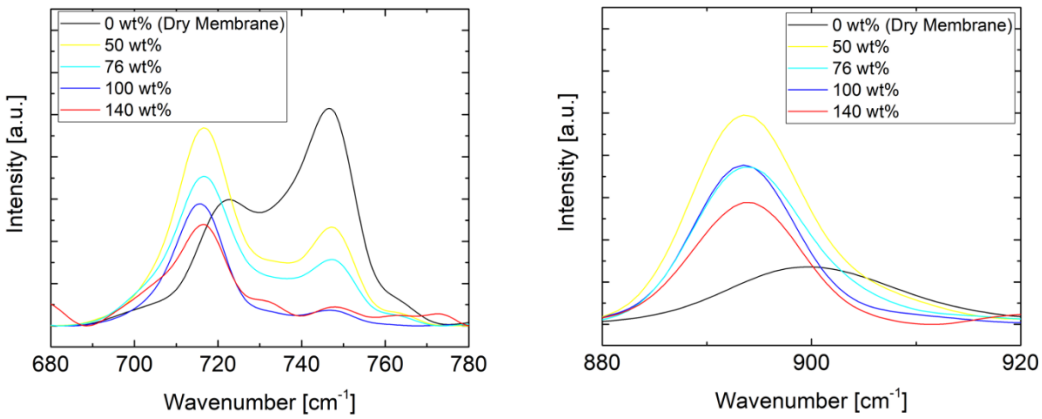

Figure S10. Raman spectra of the (**1b**) containing different amounts of plasticizer. Li-EC (730 cm^{-1}) and Li-sulfonamide (744 -747 cm^{-1}).(Tchitchekova et al., 2017), Related to Figure 5.

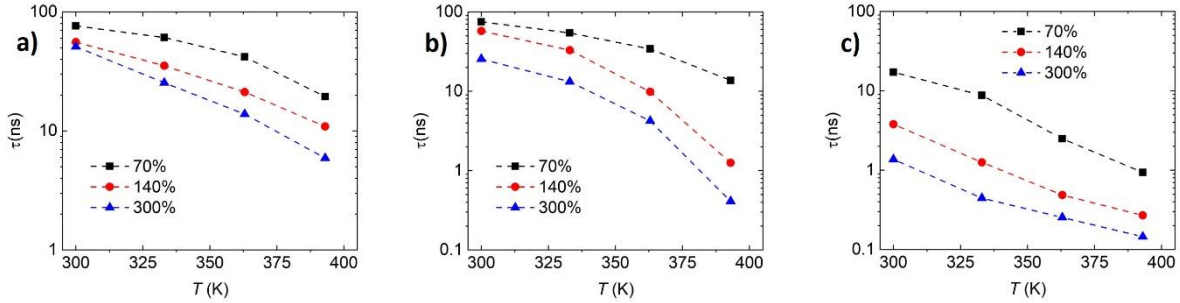

Figure S11. Residence times of Li^+ within the first coordination shell of a) O_{anion}; b) O_{amide} and c) $O_{solvent}$ in (**1b**)., Related to Figure 5.

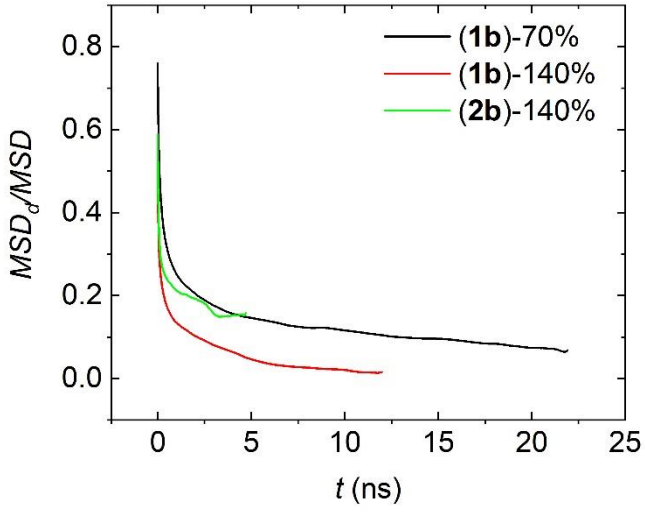

Figure S12. Contribution of Li^+ diffusion occurring along polymer chains without dissolution into solvent phase in relation to the total Li^+ mobility, Related to Figure 5.

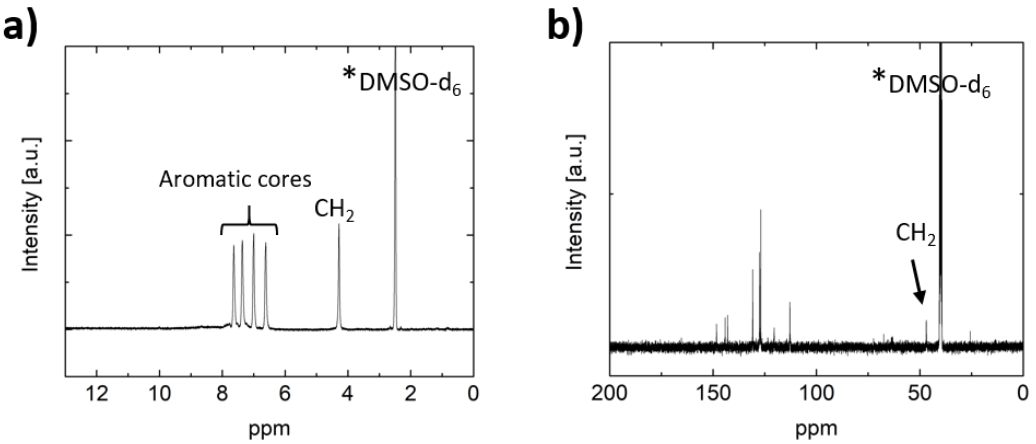

Figure S13. a) ^{1}H and b) ^{13}C liquid NMR spectra of (**3**), Related to Figure 7a.

Table S1. Membrane specifications of plasticized PVdF-HFP based blend type SIPE compared in Figure 7 (main paper). Reference labeling also refers to the numbers in the main paper, Related to Figure 1.

Ref.	***PVdF-HFP:SIPE ratio (wt:wt)***	***Plasticizer and ratio (v:v)***	***Anion***	***Position of anion***	***Polymer characterisitcs***	***Polymer/ Membrane fabrication & Morphology***
(Liu et al., 2016)	1:1	EC:PC, 1:1	$-SO_2N^-SO_2C$	Side chain	(1) Polyamide, Aromatic backbone	Solution casting, porous
					(2) Polymide, Linear + aromatic backbone	Solution casting, dense
(Pan et al., 2016)	3:2	EC:PC, 1:1	$-SO_2N^-SO_2C_6H_4CF_3$	Side chain	Cyclic Imide linker	Solution casting, dense
(Chen et al., 2018)	1:1	EC: DMC, 1:1	$-SO_2N^-SO_2CF_3$	Side chain	Ethylene alcohol backbone, grafted side chain	Solution casting, porous
(C. Li et al., 2019)	1:1	EC: DMC, 1:1	$-SO_2N^-SO_2-$	Backbnone	Aromatic polyamide, SO_2 moieties	Electrospinning, porous
(Dong et al., 2018)	1:1	EC: DMC, 1:1	$-SO_2N^-SO_2-$	Backbnone	Aromatic polyamide, SO_2 moieties	In situ polymerization, solution casting, porous
(Z. Li et al., 2018)	1:1	EC: DMC, 1:1	$-SO_2N^-SO_2CF_3$	Side chain	Cyclic Imide linker	Solution casting, dense
(Zhang, Rohan, et al., 2014)	1:1	EC:PC, 1:1	$-SO_2N^-SO_2-$	Backbone	Aromatic polyamide, SO_2 moieties	Solution casting, porous
(Sun et al., 2014)	1:2	EC:PC, 1:1	$-SO_2N^-SO_2-$ and SO_3^-	Backbone	Aromatic polyamide	Solution casting, porous

(Zhang, Lim, et al., 2014)	1:1	EC:PC, 1:1	$-SO_2N^-SO_2C_6H_5$	Side chain	Aromatic +linear polyamide	Solution casting, dense
(Qin et al., 2015)	1:1	EC: DMC, 1:1	BO_4^-	Backbone	Aromatic polyamide	Solution casting dense
(Zhang et al., 2017)	1:1	EC:PC, 1:1	$-SO_2N^-SO_2-$	Backbone	Aromatic polyamide	Solution casting, porous
(Rohan et al., 2015)	1:1	EC:PC, 1:1	(N^-)	--	Melamine	Solution casting, porous
(**2b**)	1:1	EC:PC, 1:1	$-SO_2N^-SO_2-$	Backbone	Aromatic polyamide, SO_2 moieties	Solution casting, porous
[48]	1:1	EC:PC, 1:1	$-SO_2N^-SO_2-$	Backbone	Aromatic polyamide, $C(CF_3)_2$ moieties	Solution casting, dense
(**1b**)	1:3	EC:PC, 1:1	$-SO_2N^-SO_2-$	Backbone	Aromatic polyamide, $C(CF_3)_2$ moieties	Solution casting, dense
(**3b**)	1:3	EC:PC, 1:1	$-SO_2N^-SO_2-$	Backbone	Aromatic, polyamine,$C(CF_3)_2$ moieties	Solution casting, dense

Table S2. Influence of chemical modifications on the dynamical properties (at 363K for the values obtained by MD simulations and 313K for the experimental values), Related to Figure 6 and Figure 7.

Compound	Fraction of free Li^+ (%)		D_{Li} (10^{-11} m^2/s)		σ_{Li}+(mS/cm)	
	MD	EXP	MD	EXP	MD	EXP
(1b)	32.1 ± 2.0	29.0 ± 4.0	8.6	8.4± 0.1	1.4	0.7
(2b)	26.8 ± 2.0	--	6.7	--	1.1	0.5
(3b)	39.5 ± 1.9	45± 4.0	12.2	8.7 ± 0.1	1.9	1.4

Note that, as discussed in our previous study, lithiation and subsequent purification of lithiated compounds is challenging for single ion conductors. The poor solubility of (**2**) in aprotic polar solvents (including THF) causes reproducibility issues.(Borzutzki et al., 2019) Strong variations in the lithiation degrees were detected between different batches (20%-93% applying ICP-OES). Nonetheless, due to

frequent investigation of this compound(Zhang et al., 2014; Pan et al., 2015; J. Dong et al., 2018; Zhang et al., 2018; Li et al., 2019) it was chosen for this study. To obtain highly pure and anhydrous products as well as to ensure comparability with (**1**) and (**2**), the lithiation process was performed as described rather than by LiOH in aqueous media as reported in other studies. A batch where a lithiation degree of 9% was achieved, was utilized for all experiments in this work, though the material and thus the experimental characterization was limited therefore not enabling to determine the Li ion diffusion coefficient (where >1g of material is needed) and also not allowing cell performance investigation.

Transparent Methods:

1. Molecular dynamics simulations

1.1. *Systems and force field*

The compositions of the simulated systems are given in Table S3. For systems with different polymer structure/architecture (**1**, **2**, and **3**), the number of solvent molecules remains unchanged for each given weight fraction of solvent.

Table S3. Composition of simulated systems, Related to Figure 4.

wt % of solvent	N_polyanion	N_PVdF-HFP	N_Li	N_EC	N_PC
70	16	4	80	375	325
140	16	4	80	750	650
300	16	4	80	1600	1400

In the APPLE&P force filed, the total energy is comprised of two contributions: non-bonded interactions $U^{NB}(r)$ and valence interactions, shown in equation S1. Since all chemical bonds are constrained via SHAKE algorithm, only potentials for bend, dihedral and out-of-plane dihedrals are included.

$$U^{tot}(r) = U^{NB}(r) + \sum_{bends} U^{BENDS}(\theta_{ijk}) + \sum_{dihedrals} U^{DIHEDRALS}(\emptyset_{ijkl}) \quad \text{(S1)}$$

The potentials for non-bonded interactions are comprised of repulsion-dispersion (RD) van der Waals interactions $U^{RD}(r)$, classical electrostatic potentials $U^{coul}(r)$ and interactions involving induced dipoles $U^{pol}(r)$. The details for each term are given in equation S2 with r_{ij} being the distance between atom *i* and atom *j* of types α and β, respectively. $A_{\alpha\beta}$, $B_{\alpha\beta}$ and $C_{\alpha\beta}$ are the force field parameters describing specific pairwise interaction. *D* is a constant of $5 \times \frac{10^{-5} Kcal}{mol}$ establishing the strong repulsive wall at short distances between *i* and *j*. The partial atomic charges of *i* and *j* are represented by q_i and q_j while ϵ_0 is the permittivity of vacuum. $\vec{\mu}_i$ is the induced dipole moment on an atom *i*, and $\vec{E}_i^0$ is the electric field at the location of atom *i*.

$$U^{NB}(r) = U^{RD}(r) + U^{coul}(r) + U^{pol}(r) =$$

$$\sum_{i>j}\left(A_{\alpha\beta}\exp\left(-B_{\alpha\beta}r_{ij}\right)-C_{\alpha\beta}r_{ij}^{6}+D\left(\frac{12}{B_{\alpha\beta}r_{ij}}\right)^{12}\right)+$$

$$\sum_{i>j}\left(\frac{q_i q_j}{4\pi\epsilon_0 r_{ij}}\right)-\frac{1}{2}\sum_{i}\vec{\mu}_i\vec{E}_i^{0} \quad \text{(S2)}$$

Additionally, equations S3, S4 and S5 describe interactions for bends, dihedrals and out-of-plane dihedrals, respectively. θ_{ijk} is the instantaneous bend angle, while θ_{ijk}^{0} is the equilibrium angle of the corresponding bend and $k_{\alpha\beta\gamma}^{BEND}$ is the force constant of the bend. Subscripts, α, β, γ indicate the types of atoms *i*, *j*, *k* forming the bend. In the dihedral potential, $k_{\alpha\beta\gamma\delta n}^{DIHEDRAL}$ stands for the force constant, the subscripts α, β, γ, δ define the types of atoms *i*, *j*, *k*, *l* and *n* represents the order of the cosine functions. $k_{\alpha\beta\gamma\delta}^{DEFORM}$ is the force constant of the out-of-plane deformation for an instantaneous deformation angle formed by atom *i*, *j*, *k* and *l*.

$$U^{BEND}\left(\theta_{ijk}\right)=0.5\times k_{\alpha\beta\gamma}^{BEND}\left(\theta_{ijk}-\theta_{ijk}^{0}\right)^{2} \quad \text{(S3)}$$

$$U^{DIHEDRALS}\left(\emptyset_{ijkl}\right)=\sum_{n}0.5\times k_{\alpha\beta\gamma\delta n}^{DIHEDRAL}\left(1-\cos\left(n\emptyset_{ijkl}\right)\right) \quad \text{(S4)}$$

$$U^{DEFORM}\left(\emptyset_{ijkl}\right)=\sum_{n}0.5\times k_{\alpha\beta\gamma\delta}^{DEFORM}\left({\emptyset_{ijkl}}^{2}\right) \quad \text{(S5)}$$

The parameters for each atom type are presented in Table S4, with the corresponding chemical representations given in Figure 14.

Table S4. Parameters of force field utilized for simulations, Related to Figure 4.

	A(kcal/mol)	B($Å^{-1}$)	C(kcal/mol/ $Å^6$)	Atomic Mass	Charge (e)	Polarizability
H1	5352.3	4.3646	22.59	1.008	0.1079	0.35
Hn	7584.2	5.2846	8.23	1.008	0.2318	0.21
Li	17000.0	6.0000	1.06	6.941	1	0.03
C1	97431	3.6222	519.87	12.011	0	0.9
C2	97431	3.6222	519.87	12.011	0.06	0.9
C3	97431	3.6222	519.87	12.011	0.12	0.65
C4	97431	3.6222	519.87	12.011	0.18	0.65
Cc1	33749.8	3.2995	618.32	12.011	-0.2947	1
Cc2	33749.8	3.2995	618.32	12.011	-0.2688	1.4
Cc3	33749.8	3.2995	618.32	12.011	-0.1079	1.4

Cc4	33749.8	3.2995	618.32	12.011	-0.1052	1
Cc5	33749.8	3.2995	618.32	12.011	-0.0687	1.4
Cc6	33749.8	3.2995	618.32	12.011	0.0458	0.55
Cc7	33749.8	3.2995	618.32	12.011	0.0542	1.4
Cc8	33749.8	3.2995	618.32	12.011	0.3218	1
Cg	33749.8	3.2995	618.32	12.011	0.1199	0
Cm	108283	3.6405	560.53	12.011	0.18	0.65
N1	39091.8	3.3158	833.48	14.007	-0.5472	1.45
N2	39091.8	3.3158	833.48	14.007	-0.0324	1
O=1	15923.1	3.6446	239.07	15.999	-0.4055	1
O=2	15923.1	3.6446	239.07	15.999	-0.3383	1.19
F	7117.9	3.4174	150.72	18.998	-0.06	0.6
S-	56881.7	2.8261	2639.27	32.066	0.6446	0.9
Cce	97431	3.6222	540.66	12.011	0.3852	0.1
Ce1	97431	3.6222	540.66	12.011	-0.0163	0.5
Ce2	97431	3.6222	540.66	12.011	0.0246	0.5
Ce3	97431	3.6222	540.66	12.011	0.1543	0.5
Cme	108283	3.6405	582.95	12.011	-0.1264	0.9
Oe1	15923.1	3.6446	248.63	15.999	0.2985	0.81
Oe2	15923.1	3.6446	248.63	15.999	0.3217	0.81
O=e	15923.1	3.6446	248.63	15.999	-0.4282	1.5
He1	5352.3	4.3646	23.49	1.008	0.026	0.35
He2	5352.3	4.3646	23.49	1.008	0.05	0.35
He3	5352.3	4.3646	23.49	1.008	0.0576	0.35

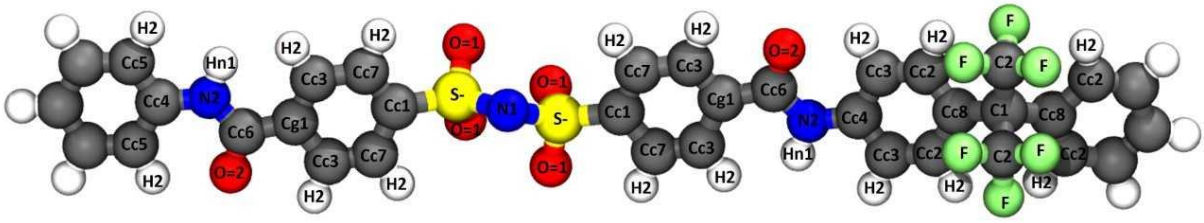

Figure S14. Molecular structure of (**1**) and atom labels from the force field, Related to Figure 4.

1.2 Simulation and analysis protocols

System for MD simulations were comprised of sixteen single-ion conducting polymer chains with n=5, four PVDF-HFP chains and 700-3000 solvent molecules depending on the solvent content. All simulations were conducted using Atomistic Polarizable Potentials for Liquids, Electrolytes, and Polymers (APPLE&P) force field.(Oleg Borodin, 2009; Dmitry Bedrov et al., 2018). The repulsion-dispersion interactions were calculated within a cut-off distance of 15.0 Å. All charge-charge

interactions were calculated using Ewald summation(Yeh & Berkowitz, 1999) with the cut-off distance for the real-space component of 15.0 Å. The interaction due to polarizability, i.e. the response of electric cloud to the electric field induced by neighboring point charges, has been calculated via the induced dipole model.(Oleg Borodin, 2009; D. Bedrov et al., 2019) The Thole screening parameter of 0.2 was utilized to avoid polarizability 'catastrophe' at short separations.(Thole, 1981; O. Borodin & Smith, 2006) The charge-induced dipole interactions were calculated using Ewald summation, while induced dipole–induced dipole interactions were truncated at the cut-off distance and applying smooth tapering that brings forces and energies to zero starting from 14.5 Å separations. All chemical bonds were constrained via SHAKE algorithm.(Palmer, 1993) To enhance computational efficiency, a multiple time step integration approach has been applied. A 0.5 fs time step has been used for the calculation of bonds, bends, and out-of-plane deformations, a 1.5 fs time step was used for the calculation of torsions and non-bonded interactions within the short range (8 Å cut off), while a 3.0 fs time step was employed for the calculation of remaining non-bonded interactions and the reciprocal part of the Ewald summation for electrostatic interactions.

Consistent with our previous simulations of polymer membranes, the preparation of the systems followed a multi-step equilibration process.(D. Dong et al., 2018) The initial configuration for each system was prepared by randomly putting all polymer chains, Li^+ cations and solvent molecules into a large (800 Å) simulation cell. A short-time simulation (6 ps) was conducted to relax intramolecular geometries and conformations, followed by a 300 ps simulation with cell shrinking to obtain reasonable cell dimensions. Then, the systems were subjected to simulation in the NVT (canonical) ensemble at elevated temperature, i.e. 1000 K, for 3 ns to allow relaxation of polymer chain conformations.(Oleg Borodin, 2009) Afterwards, each system was cooled down at a constant cooling rate of 100 K/ns to a series of target temperatures, including 300 K, 333 K, 363 K, and 393 K. Thereafter, equilibration runs over 10ns were conducted using an NPT (isobaric, isothermal) ensemble, in which the Nose-Hoover thermostat and barostat were used to control temperature and pressure,

respectively.(Frenkel & Smit, 2001) Production runs were conducted over 30-40 ns, depending on temperature.

The radial distribution functions were calculated via eq. S6:

$$g(r) = \frac{n(r)}{\rho 4\pi r^2 \Delta r} \quad \text{(S6)}$$

where $n(r)$ represents the number of species at distance *r* and ρ is the average density of those species. $g_{Li-N_{anion}}(r)$ is given in Figure Sa. Consistent with previous investigations on Li-TFSI binding in PEO based electrolytes, two Li coordinating structures are observed for the range 3 Å - 5 Å. For different solvent contents, the monodentate coordination dominates the Li-O_{anion} coordination.

The diffusion coefficients *D* were determined by fitting the long-time limit of mean square displacement (MSD) following eq. S7, where *N* is the total number of molecules, $R_i(t)$ the coordinate of molecules *i* at time *t*, and < > is the ensemble average.

$$MSD(t) = 6Dt = < \frac{1}{N} * \sum_{i}^{N} [R_i(t) - R_i(0)]^2 > \quad \text{(S7)}$$

To evaluate the contribution of Li^+ movement along the polymer chain to the overall Li^+ conductivity, the decomposed MSD is defined in equation S8

$$MSD_d(t) = < \frac{\sum_{i=1}^{N} s_i(t) * [R_i(t) - R_i(0)]^2}{\sum_{i=1}^{N} s_i(t)} > \quad \text{(S8)}$$

in which *s(t)* is a binary pre-factor to determine if selected Li^+ coordinates with the polymer (primarily polymer oxygen), with $s(t)$=1 if Li^+ coordinates with polymer oxygen atoms within the time *t*, and $s(t)$=0, otherwise. The MSD_d/MSD ratio at 363 K is given in Figure S. For different solvent contents, the contribution from Li^+ diffusion along the polymer chain is minimal.

The analysis of residence times was conducted by calculation of autocorrelation functions (ACF) as defined in eq. S9

$$ACF(t) = \frac{< H_{ij}(t) H_{ij}(0) >}{< H_{ij}(0) H_{ij}(0) >} \quad \text{(S9)}$$

where $H_{ij}(t)$ shows whether or not atom *j* is inside the correlational region of specie *i* at time *t*. If the atom is within the correlation region then $H_{ij}(t) = 1$, otherwise, $H_{ij}(t) = 0$. The *ACF(t)* obtained from MD simulations is fit with the Kohlrausch-Williams-Watts(KWW) function:

$$P\ (t) = Aexp\left(-\left(\frac{t}{\tau_{KWW}}\right)^{\beta}\right) \quad (S10)$$

where A, τ_{KWW} and β are fitting parameters. Integratioin of *P(t)* from t = 0 to t→∞ yields the characteristic residence time τ:

$$\tau = \int_0^{\infty} P(t)dt. \quad (S11)$$

The ionic conductivity was calculated from the charge-charge displacement correlations as:

$$\lambda = \lim_{t\to\infty} \frac{e^2}{6tVk_BT} \sum_{ij}^{N} Z_i Z_j < [R_i(t) - R_i(0)]\big[R_j(t) - R_j(0)\big] > \qquad (S12)$$

where λ denotes total ionic conductivity, *e* is the magnitude of the unit charge of electron, *t* is time, V is volume of the simulation cell, k_B is the Boltzmann constant, Z_i and Z_j are charges of species *i* and *j*, *R(t)* and *R(0)* are the ion locations at time *t* and time origin, respectively. The conductivity was extracted from simulations by fitting the long-time data from eq. S12.

2. Experimental section

2.1. Materials

P-toluenesulfonamide (97 %), *p*-toluenesulfonyl chloride (97 %), potassium permanganate ($KMnO_4$,), lithium hydroxide monohydrate, calcium chloride, 4,4'-Diaminodiphenyl sulfone (97 %), *N*-methyl-2-pyrrolidone (NMP, anhydrous, 99.8 %), pyridine (anhydrous, 99.8 %), dimethylacetamide (DMAC, anhydrous, 99.8%), tetrahydrofuran (THF, anhydrous, 99.8 %), $LiAlH_4$ (95 %), lithium bis(trimethylsilyl)amide solution (1M in THF), terephthalic acid (98 %) were obtained from Sigma Aldrich, Germany. 4,4'(Hexafluoroisopropylidene)dianiline (98 %) was purchased from TCI Europe. Poly(vinylidene difluoride-co-hexafluoropropylene) PVdF-HFP (Kynar FLEX LBG) was purchased from Arkema, Austria. Concentrated hydrochlorid acid, methanol (AR), dimethylsulfoxide (DMSO, AR) and

triphenylphosphite (TPP, AR) were acquired from VWR. Ethylene carbonate (EC) and propylene carbonate (PC) were purchased from BASF, Germany. $LiNi_{1/3}Co_{1/3}Mn_{1/3}O_2$ and $LiFePO_4$ were obtained from Shanshan (China), carbon black (Super C65) from Imerys Graphite and carbon and polyvinylidene difluoride (PVdF, Solef 5130) from Solvay, Belgium. Calcium chloride was dried at 180 °C under reduced pressure (10^{-3} mbar) for 48 hours, 4,4'(Hexafluoroisopropylidene)dianiline was dried at 100 °C under reduced pressure (10^{-3} mbar) for 24 hours.

2.2. Synthesis

*2.2.1. Synthesis of (**1**) and (**2**):*

Synthesis of (**1**) was performed based on (Borzutzki et al., 2019).^{1}H NMR (400 MHz, 293 K, DMSO-d_6): δ = 10.60 (s, 4H, NH_2), 7.97 (d, *J*= 8.33 Hz, 4H, Ar-H), 7.91 (d, *J*= 8.84 Hz, 4H, Ar-H), 7.82 (d, *J*= 8.11 Hz, 4H, Ar-H), 7.35 (d, *J*= 7.86 Hz, 4H, Ar-H). Synthesis of (**2**) was performed equally using 4,4'-Diaminodiphenyl sulfone instead of 4,4'(Hexafluoroisopropylidene)dianiline. ^{1}H NMR (400 MHz, 293 K, DMSO-d_6): δ = 10.75 (s, 4H, NH_2), 8.02 (m, 4H, Ar-H), 7.95 (m, 8H, Ar-H), 7.84 (m, 4H, Ar-H).

*2.2.2. Synthesis of (**3**):*

Reduction of (**1-H**):

In a Schlenk flask equipped with a condenser, 1.000 g of (**1-H**) (1.464 mmol) was dissolved in 60.00 ml of anhydrous THF at RT. 0.264 g (2.4 eq., 6.960 mmol) of $LiAlH_4$ were slowly added to the solution. The solution was heated to 80 °C and stirred for 72 h under reflux yielding a green/grey suspension. After that, the flask was cooled to RT and the excess of $LiAlH_4$ was reacted by slowly adding H_2O to the reaction mixture, thereby changing its colour to light yellow. Upon addition of HCl the side products were dissolved whereas the product precipitated from the solution. The final product (**3-H**) was obtained by filtration and drying under vacuum at 100 °C in a quantitative yield. Complete removal of Al species was confirmed by TXRF (Al < 0.05 %, Cl < 0.05 %). ^{1}H NMR (400 MHz, 293 K, DMSO-d_6): δ = 7.65 (d, *J*= 7.56 Hz, 4H, Ar-H), 7.39 (d, *J*= 7.51 Hz, 4H, Ar-H), 7.02 (d, *J*= 7.87 Hz, 4H, Ar-H), 6.65 (d, *J*= 7.98 Hz, 4H, Ar-H), 4.30 (s, 4H, CH_2).

Lithiation of (**3-H**)

0.900 g of (**3-H**) was dissolved in 100.00 ml anhydrous THF. The reaction mixture was placed in an ice bath and stirred. 1.45 ml of 1 M lithium bis(trimethylsilyl)amide in THF were slowly added to the solution whereby (**3**) precipitated from the solution. The solution mixture was allowed to stir for another 6 h upon cooling before it was filtrated to remove the solvent and bis(trimethylsilyl)amide. The final product was dried for 24 h under reduced pressure and at 80 °C. The final product was obtained in a quantitative yield (95 %). ^{1}H NMR (Figure S) confirmed the complete removal of solvent and by products. Full lithiation was confirmed by inductively coupled plasmaoptical emission spectroscopy (ICP-OES).

2.3. Preparation of the single-ion conducting polymer electrolyte membrane

Polymer membranes were prepared by a solution cast method. For the blend membranes 125 mg of PVdF-HFP and 375 mg of the single-ion conducting polymer (**1**), (**2**) or (**3**) were dissolved in 9 ml DMAC at 60 °C. Membranes composed of (**1**), (**2**), indicated as (**1-m**) and (**2-m**) respectively and PVdF-HFP were fabricated dissolving 500 mg of polymer in 9 ml DMAC at 60 °C.

The solution was cast into a Teflon petri dish and the solvent was slowly evaporated by placing the petri dish into an oven at 80 °C overnight, then applying vacuum to the oven for another 24 h. For the blend membranes, from the obtained homogenous membrane (thickness 80 µm ± 2 µm) disks of 12 mm or 13 mm were cut and further dried at 100 °C under vacuum (Schlenk line) for 48 h. Whereas (**1-m**), (**2-m**) and PVdF-HFP membranes were analyzed in dry state, the blend membranes were then soaked in EC: PC (1:1, v: v) solvent solution. The corresponding weight uptake/solvent uptake (SU) was determined based on the equation:

$$SU = \frac{w_s - w_0}{w_0} * 100\ \% \qquad (S13)$$

with w_s and w_0 denoting the weight of the swollen and dry membrane, respectively.

To achieve membranes of different weight uptakes (Figure S11 and S13), the mass of the dry membrane was determined and a defined mass of EC: PC was added on top of the membrane placed in a glass vial. The membranes where allowed to take up the solvent over a period of 48 h. The wt%

value given in Figure S11 and S13 are based on the mass finally determined after the soaking period. Note that the "natural solvent uptake" of 140 wt% for (**1b)** and 150 wt% for (**2b)** are obtained when placing the membrane in an excess of EC: PC for 48 hours, dabbing it on a tissue to remove excessive EC: PC on the surface and determining the weight of the membrane. The average weight of the dry membranes was 6.0 mg cm^{-2} (corresponding to 14.4 mg cm^{-2} in a plasticized state in case of 140 wt% SU for (**1b**).

2.4. Preparation of cathodes

$LiNi_{1/3}Co_{1/3}Mn_{1/3}O_2$ (NMC111) and $LiFePO_4$ based cathodes were prepared by firstly dissolving 0.12 g (7.5 wt%) PVdF in 6 ml NMP and stirring the solution overnight. Subsequently, 0.12 g (7.5 wt%) of carbon black, 0.08g (5 wt%) of lithiated terephthalic acid and 1.28 g (80 wt%) of NMC or LFP, respectively were added and stirred for another 30 min. The viscous solution was transferred to a swing mill (MM 400 (Retsch Technology, Haan, Germany) where it was stirred for 30 min at a frequency of 30 Hz. Aluminum foil used as current collector was wiped with ethanol to remove surface contaminations. Then, the cathode slurry was cast onto the Al using a doctor blade technique setting the gap width to 50 µm. The obtained coating was dried at 80 °C overnight followed by further drying at 80 °C under vacuum. The electrodes were calandared and the final electrode coating thickness was 13 µm and its mass loading was 2.8 mg cm^{-2}. After punching of the electrodes (12 mm disk), they were further dryed at 80 °C under vacuum for 48h.

2.5. Characterization methods

^{1}H and ^{13}C liquid NMR spectra were recorded at 293 K on a BRUKER 400 AVANCE III HD instrument using deuterated dimethyl sulfoxide (DMSO-d6) as reference signal for the ^{1}H spectra.

Pulsed field gradient nuclear magnetic resonance (PFG-NMR) was performed at a BRUKER 200 AVANCE III spectrometer equipped with a (doubly tuned $^{7}Li/^{1}H$) 5 mm coil at 40 °C ($\pm$ 0.1 °C). For external calibration (0 ppm) a solution of 0.25 M LiCl in H_2O was utilized. For the measurement 4750 scans at gradient strengths varying g from 35 – 1050 G cm^{-1} were recorded. The gradient pulse length δ was set to 1 ms and the diffusion time Δ to 40 ms. Self-diffusion coefficients D_{Li^+} of the lithium species were derived from a stimulated echo sequence ("diffSte") after fitting the attenuated signal

amplitude to the Stejskal-Tanner equation, which describes the case of rather ideal (“free”) isotropic diffusion:

$$I = I_0 * e^{\left(-D\,\gamma^2\delta^2\,g^2\left(\Delta-\frac{\delta}{3}\right)\right)} \quad (S14)$$

with I being the signal intensity, I_0 being the initial signal in absence of a magnetic field gradient and γ being the gyromagnetic ratio. The software BRUKER Topspin 3.5 and BRUKER Dynamics Center 2.5 where applied for the data analysis.

For ICP-OES measurements the device Spectro ARCOS EOP (Spectro Analytical Instruments GmbH, Kleve, Germany) was used. Prior to the measurement, the polymer was dissolved by a microwave-assisted acid digestion (Anton Paar Multiwave Pro, Graz, Austria).

TXRF measurements were performed using a Picofox S2 system equipped with the Spectra 7.5 software (Bruker Corporation, Billerica, MA, USA) placing the polymer on a quartz glass carrier from Bruker Corporation.

For determination of the ionic conductivity of the polymer membranes electrochemical impedance spectroscopy (EIS) was conducted using a NOVOCONTROL alpha-S-spectrometer. The impedance spectra were recorded in a temperature range of -20 °C and 80 °C in 10-degree steps whereby the temperature ramp was applied multiple times to proof reversible behavior. An alternating voltage signal with an amplitude of 5 mV over a frequency range from 10^{-1} to $4*10^7$ Hz was applied. For the measurement the polymer membrane was punched to a 12 mm diameter disk and assembled in a coin cell (two electrode configuration(Nölle et al., 2019)) between two stainless steel electrodes. From the plateau region of the frequency-dependent real part of the complex conductivity, the DC conductivity values were extracted.

For determination of the lithium- ion transference number (t^+) the measurement technique proposed by Evans et al.(Evans, Vincent, & Bruce, 1987) was used. Therefore, the membrane was assembled in a symmetrical coin cell setup between two non-blocking lithium metal electrodes. Potentiostatic polarization and complex impedance (in the frequency range between 1 mHz and 1 MHz

with a DC polarization voltage ΔV of 10 mV) were collected at 60 °C using a VSP instrument (Bio-Logic Science Instruments) device. Subsequently, the lithium ion transference number was determined by

$$t_{Li}^{+} = \frac{I_S(\Delta V - I_0 R_0)}{I_0(\Delta V - I_S R_S)} \quad (S15)$$

with $I_O and\ I_S$ being the initial and steady state current and $R_O and\ R_S$ being the initial and steady state resistances of the interfaces.

The electrochemical stability window of the polymer membrane was determined using a VSP instrument (Bio-Logic Science Instruments). A three electrode cell setup with lithium as counter and reference electrode and platinum as working electrode for oxidative or copper as working electrode for reductive stability, respectively, was utilized. A scan rate of 80 μV s^{-1} was applied in the potential range between -0.5 V and 6 V (vs. Li|Li^+) and at 20 °C .

Cycling investigations were performed on the battery cell analysis system Maccor 4000 (USA). Cycling of NMC111||Li full cells was performed between 3.0 V and 4.3 V (constant current, CC). For symmetrical Li||Li cells a current density of 0.1 mA/cm^2 was applied for one hour. The experiments in two electrode configuration(Nölle et al., 2019) were conducted in a climate chamber held at a constant temperature of 60 °C.

Electrochemical impedance spectra of the assembled NMC111||Li full cells were recorded on a VSP instrument (Bio-Logic Science Instruments) by application of a DC polarization voltage ΔV of 10 mV in a frequency range between 1 mHz and 1 MHz. During the measurments the cells were kept in a climate chamber. The otained compley impedance spectra were fitted by the software *RelaxIS* utilizing an equivalent circuit demonstrated in Figure 9a in the manuscript.

Raman spectra were recorded on a Senterra Raman spectrometer from Bruker Optics Inc using a laser wavelength of 785 nm, a grating with 400 lines mm^{-1} and an aperture with a 50 x 1000 μm sized slit. The laser power was adjusted to 10 mW. Both, laser and spectrometer were calibrated with a neon lamp. The detector was a CCD (charge coupled device) detector with 1024x 256 pixels, which was thermoelectrically cooled to -65 °C. A 50x objective was used as microscope. For collection of the spectra, 15 integrations were carried out with an integration time of 10 s.

Attenuated total reflection Fourier transform infrared (ATR FTIR*)* spectroscopy was performed on a Bruker Vertex 70 in a spectral range between 400 cm^{-1} and 4000 cm^{-1} with a spectral resolution of 1 cm^{-1} and 512 scans.

Scanning electron microscopy (SEM) was investigated on a Zeiss Auriga electron microscope (Carl Zeiss Microscopy GmbH) using an accelerating voltage of 3 kV.

Small angle X-ray scattering (SAXS) experiments were performed in the Q-range from 0.1 to 1.7 nm^{-1} at the Gallium Anode Low-Angle X-ray Instrument (GALAXI) at Forschungszentrum Jülich.(Kentzinger, Krutyeva, & Rücker, 2016) The incident wavelength is 1.34 Å and the detector distance was set to 3.5 m. All swollen samples were sealed in glass capillaries of 2 mm inner diameter. The dried samples were measured without capillaries. All SAXS measurements were performed at room temperature. The data were background corrected and calibrated to absolute intensities. Data analysis has been done using the Python based software *jscatter*.(Biehl, 2019)

Atomic Force Microscope (AFM) measurements were performed in an Agilent 5400 system using the PicoView 1.2 software version. Imaging was performed in AC mode tune with standard soft cantilevers with a resonance frequency of Δf =72-74 kHz in air and in ambient temperature. For data analysis Gwyddion 2.5 and Image *J* were used.

XRD measurements were performed with a Bruker D8 Advanced (Cu Kα radiation, 0.154 nm) between 6° and 55° 2θ with a step size of 0.019° and a step time of 1 s.

2.6 Experimental consideration of the degree of ion dissociation

The degree of ionic dissociation was calculated based on the experimentally obtained ionic conductivity σ_{DC}, the transference number t_{Li^+} and the Li diffusion coefficient $D_{Li^+_{PFG}}$ (PFG-NMR). A theoretical lithium ion self-diffusion coefficient $D_{Li^+_{calc}}$ and the ion mobility $\mu_{Li^+_{calc}}$ are estimated by the Nernst Einstein and Einstein equations whereby the lithium- ion transference number t_+ was taken as a correction factor to obtain $\sigma_{Li^+_{calc}}$ which is the content of Li ions contributing to the measured overall conductivity σ_{DC}, yielding:

$$\mu_{Li^+_{calc}} = \frac{\sigma_{Li^+_{calc}}}{ne} \approx \frac{\sigma_{DC} * 0.9}{ne} \quad (S16)$$

$$D_{Li^+_{calc}} \approx \frac{kT}{ne^2}\,\sigma_{Li^+_{calc}} \quad (S17),$$

where *n* is the charge carrier density, *e* is the elemental charge, *k* is the Boltzmann constant, *T* the temperature. The charge carrier density *n* is estimated based on stoichiometric and geometric parameters (thickness, area, weight) of the rather homogenous SIPE membranes. The ratio of $D_{Li^+_{calc}}/D_{Li^+_{PFG}}$ then yilds the degree of ion dissociation..

References

Bedrov, D., Pequemal, J.-P., Borodin, O., MacKerell, J. A. D., Roux, B., & Schroeder, C. (2019). Polarizable Molecular Dynamics Simulations of Ionic and Polar Systems. Chemical Reviews, 119, 7940–7995.

Bedrov, D., Piquemal, J.-P., Borodin, O., Mackerell, A. D., & Schröder, C. (2018). Molecular Dynamics Simulations of Ionic Liquids and Electrolytes Using Polarizable Force Fields. Chemical Reviews, 119, 7940–7995.

Biehl, R. (2019). Jscatter, a program for evaluation and analysis of experimental data. PLoS ONE, 14, 1–18.

Borodin, O. (2009). Polarizable force field development and molecular dynamics simulations of ionic liquids. Journal of Physical Chemistry B, 113, 11463–11478.

Borodin, O., & Smith, G. D. (2006). Development of Many−Body Polarizable Force Fields for Li-Battery Components: 1. Ether, Alkane, and Carbonate-Based Solvents. Journal of Physical Chemistry B, 110, 6279–6292.

Borzutzki, K., Thienenkamp, J., Diehl, M., Winter, M., & Brunklaus, G. (2019). Fluorinated polysulfonamide based single ion conducting room temperature applicable gel-type polymer electrolytes for lithium ion batteries. Journal of Materials Chemistry A, 7, 188–201.

Dong, D., Zhang, W., Barnett, A., Lu, J., van Duin, A. C. T., Molinero, V., & Bedrov, D. (2018). Multiscale Modeling of Structure , Transport and Reactivity in Alkaline Fuel Cell Membranes : Molecular Dynamics Simulations. Polymers, 10, 1289.

Dong, J., Zhang, Y., Wang, J., Yang, Z., Sun, Y., Zeng, D., Liu, Z., & Cheng, H. (2018). Highly porous single ion conducting polymer electrolyte for advanced lithium-ion batteries via facile water-induced phase separation process. Journal of Membrane Science, 568, 22–29.

Evans, J., Vincent, C. A., & Bruce, P. G. (1987). Electrochemical measurement of transference number in polymer electrolytes. Polymer, 28, 2324–2328.

Frenkel, D., & Smit, B. (2001). Understanding molecular simulation: From algorithms to applications. Computational Science Series 1. Elsevier.

Gao, Q., & Scheinbeim, J. I. (2000). Dipolar intermolecular interactions, structural development, and electromechanical properties in ferroelectric polymer blends of nylon-11 and poly(vinylidene fluoride). Macromolecules, 33, 7564–7572.

Kentzinger, E., Krutyeva, M., & Rücker, U. (2016). GALAXI: Gallium anode low-angle x-ray instrument. Journal of large-scale research facilities JLSRF, 2, 61.

Li, C., Qin, B., Zhang, Y., Varzi, A., Passerini, S., Wang, J., Dong, J., Zeng, D., Liu, Z., & Cheng, H. (2019). Single-Ion Conducting Electrolyte Based on Electrospun Nanofibers for High-Performance Lithium Batteries. Advanced Energy Materials, 9, 1–9.

Mocilac, P., Osman, I. A., & Gallagher, J. F. (2016). Short C-H···F interactions involving the 2,5-difluorobenzene group: Understanding the role of fluorine in aggregation and complex C-F/C-H disorder in a 2 × 6 isomer grid. CrystEngComm, 18, 5764–5776.

Morita, M., Asai, Y., Yoshimoto, N., & Ishikawa, M. (1998). A Raman spectroscopic study of organic electrolyte solutions based on binary solvent systems of ethylene carbonate with low viscosity solvents which dissolve different lithium salts. Journal of the Chemical Society - Faraday Transactions, 94, 3451–3456.

Nölle, R., Beltrop, K., Holtstiege, F., Kasnatscheew, J., Placke, T., & Winter, M. (2019). A reality check and tutorial on electrochemical characterization of battery cell materials: How to choose the appropriate cell setup. Materials Today, accepted.

Palmer, B. J. (1993). Direct Application of Shake to the Velocity Verlet Algorithm. Journal of Computational Physics, 104, 470–472.

Pan, Q., Zhang, W., Pan, M., Zhang, B., Zeng, D., Sun, Y., & Cheng, H. (2015). Construction of a lithium ion transport network in cathode with lithiated bis(benzene sulfonyl)imide based single ion polymer ionomers. Journal of Power Sources, 283, 279–288.

Smart, B. E. (2001). Fluorine substituent effects (on bioactivity). Journal of Fluorine Chemistry, 109, 3–11.

Socrates, G. (2001). Infrared and Raman characteristic group frequencies (3rd ed.). John Wiley & Sons Ltd.

Tchitchekova, D. S., Monti, D., Johansson, P., Bardé, F., Randon-Vitanova, A., Palacín, M. R., & Ponrouch, A. (2017). On the Reliability of Half-Cell Tests for Monovalent (Li + , Na +) and Divalent (Mg 2+ , Ca 2+) Cation Based Batteries . Journal of The Electrochemical Society, 164, A1384–A1392.

Thalladi, V. R., Weiss, H. C., Bläser, D., Boese, R., Nangia, A., & Desiraju, G. R. (1998). C-H···F interactions in the crystal structures of some fluorobenzenes. Journal of the American Chemical Society, 120, 8702–8710.

Thole, B. T. (1981). Mlecular Polarizabilities Calculated with a Modified Dipole Interaction. Chemical Physics, 59, 341–350.

Yeh, I.-C., & Berkowitz, M. L. (1999). Ewald summation for systems with slab geometry. The Journal of chemical physics, 111, 3155–3162.

Zhang, Y., Chen, Y., Liu, Y., Qin, B., Yang, Z., Sun, Y., Zeng, D., Alberto Varzi, Passerini, S., Liu, Z., & Cheng, H. (2018). Highly porous single-ion conductive composite polymer electrolyte for high performance Li-ion batteries. Journal of Power Sources, 397, 79–86.

Zhang, Y., Sun, Y., Cheng, H., Rohan, R., Cai, W., Xu, G., Lin, A., Sun, Y., Lin, A., & Cheng, H. (2014). Influence of Chemical Microstructure of Single Ion Polymeric Electrolyte Membranes on Performance of Lithium Ion Batteries. ACS Applied Materials & Interfaces, 6, 17534–17542.